



# U4D: Uncertainty-Aware 4D World Modeling from LiDAR Sequences

Xiang Xu<sup>1</sup> Ao Liang<sup>2</sup> Youquan Liu<sup>3</sup> Linfeng Li<sup>2</sup> Lingdong Kong<sup>2</sup>  
Ziwei Liu<sup>4</sup> Qingshan Liu<sup>5,✉</sup>

<sup>1</sup>Nanjing University of Aeronautics and Astronautics <sup>2</sup>National University of Singapore  
<sup>3</sup>Fudan University <sup>4</sup>S-Lab, Nanyang Technological University  
<sup>5</sup>Nanjing University of Posts and Telecommunications

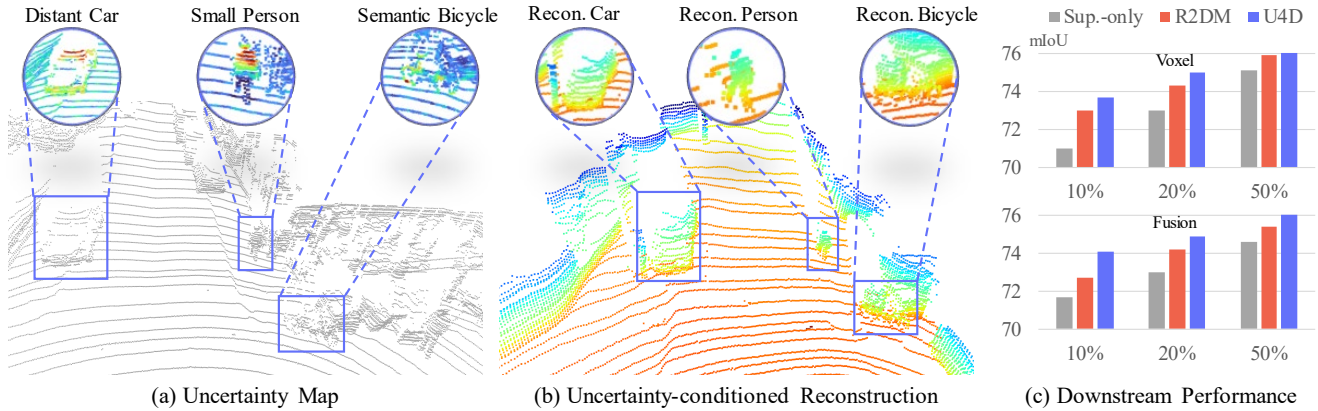


Figure 1. **Illustration of the proposed U4D framework** for uncertainty-aware LiDAR scene generation. (a) U4D first estimates the spatial uncertainty maps, highlighting regions that are challenging for perception, such as distant or partially occluded objects, small-scale instances, and semantically ambiguous areas. (b) Conditioned on these uncertainty regions, U4D performs scene completion in a “hard-to-easy” manner, progressively reconstructing the entire scene with enhanced fidelity in uncertain regions. (c) The generated uncertainty-aware scenes can further benefit downstream perception tasks by improving robustness and recognition performance.

## Abstract

Modeling dynamic 3D environments from LiDAR sequences is central to building reliable 4D worlds for autonomous driving and embodied AI. Existing generative frameworks, however, often treat all spatial regions uniformly, overlooking the varying uncertainty across real-world scenes. This uniform generation leads to artifacts in complex or ambiguous regions, limiting realism and temporal stability. In this work, we present **U4D**, an uncertainty-aware framework for 4D LiDAR world modeling. Our approach first estimates spatial uncertainty maps from a pretrained segmentation model to localize semantically challenging regions. It then performs generation in a “hard-to-easy” manner through two sequential stages: (1) uncertainty-region modeling, which reconstructs high-entropy regions with fine geometric fidelity, and (2) uncertainty-conditioned completion, which synthesizes the remaining areas under learned structural

priors. To further ensure temporal coherence, U4D incorporates a mixture of spatio-temporal (MoST) block that adaptively fuses spatial and temporal representations during diffusion. Extensive experiments show that U4D produces geometrically faithful and temporally consistent LiDAR sequences, advancing the reliability of 4D world modeling for autonomous perception and simulation.

## 1. Introduction

Modeling dynamic 3D environments from LiDAR sequences is fundamental to constructing reliable 4D world models that enable autonomous systems to perceive, simulate, and interact with the physical world over time [38, 60, 83]. LiDAR provides precise geometric and depth information, forming the basis for perception, mapping, and planning in autonomous driving [43, 44, 93], robotics [21, 53, 69], and large-scale scene reconstruction [84, 102]. However, collecting large-scale, diverse, and annotated LiDAR data remains costly and labor-intensive [16, 36, 78, 92], motivating increasing interest in generative LiDAR modeling

(✉) Corresponding author.

for scalable simulation, data augmentation, and pretraining.

Recent advances have explored LiDAR scene generation via adversarial, variational, and diffusion-based generative frameworks [7, 71, 83]. Early efforts focus on object-level point clouds [1, 17, 31, 59], whereas recent methods such as LiDARGen [108], LiDM [71], and LiDARCrafter [45] synthesize large-scale and even dynamic LiDAR scenes. Despite these advances, existing methods treat spatial regions equally during generation, ignoring the varying semantic difficulty of real-world data. This uniform assumption often causes unreliable reconstruction in geometrically or semantically complex regions, such as thin poles, moving objects, and distant surfaces, where predictive confidence is low.

We observe that reliable LiDAR world modeling requires understanding the underlying uncertainty itself. As shown in Fig. 1 (a), real LiDAR observations exhibit inherently non-uniform difficulty: while some areas are well-defined, others – such as occluded areas, small-scale structures, or semantically ambiguous regions – remain uncertain. Ignoring this asymmetry leads to geometric artifacts and temporal instability. Inspired by how humans resolve ambiguous regions before perceiving global context, we propose to model uncertainty explicitly, generating difficult regions first as structural anchors for the rest of the scene.

To this end, we propose **U4D**, an uncertainty-aware framework for 4D LiDAR world modeling. U4D leverages spatial uncertainty as a structural prior to guide scene generation. Our framework first estimates an uncertainty map from a pretrained LiDAR segmentation network to localize semantically ambiguous or geometrically unreliable regions. It then performs two sequential stages of generation: (1) an *uncertainty-region diffusion* stage, which focuses on reconstructing high-entropy regions with fine geometric fidelity, and (2) an *uncertainty-conditioned completion* stage, which synthesizes the remaining areas conditioned on these reconstructed structures (Fig. 1 (b)). The two stages share a unified latent scene representation, enabling global contextual cues to refine local uncertainty and ensuring geometric and temporal consistency across the generated 4D scenes.

To further ensure stable temporal evolution, **U4D** integrates a **Mixture of Spatio-Temporal (MoST)** block, which explicitly decomposes and adaptively fuses spatial and temporal representations within the diffusion process. This design enables the generation of LiDAR sequences that are both geometrically precise and temporally coherent. Extensive experiments on the *nuScenes* [8] and *SemanticKITTI* [5] datasets demonstrate that U4D consistently outperforms existing LiDAR generation frameworks in terms of geometric fidelity, temporal stability, and downstream generalization (Fig. 1 (c)).

The main contributions of this work are as follows:

- We introduce the first uncertainty-aware LiDAR generation framework that explicitly models spatial difficulty to

enhance reliability in 4D world modeling.

- We design a two-stage hard-to-easy generation paradigm that reconstructs uncertain regions first and then completes the full scene under these priors.
- We develop a Mixture of Spatio-Temporal (MoST) block that ensures temporal consistency across frames by adaptively balancing spatial geometry and temporal dynamics.

## 2. Related Work

**LiDAR Scene Understanding.** LiDAR sensors provide accurate geometric measurements of 3D environments. Due to the sparse and irregular nature of LiDAR point clouds, existing methods typically transform LiDAR data into alternative representations for efficient processing, including raw points [27, 67, 68, 77], bird’s-eye-view [10, 103, 104], range images [2, 33, 89, 93], sparse voxels [11, 26, 97, 99, 106], and multi-view fusion [46, 49, 79, 90, 107]. While achieving strong performance across tasks such as segmentation and detection, these methods heavily rely on large-scale annotated datasets, which are costly to acquire. To alleviate this dependency, recent works explore semi-supervised [37, 42, 85], weakly-supervised [48, 57, 91], and self-supervised [66, 73, 95, 96, 100] learning strategies, aiming to maintain high performance while reducing the need for extensive labeled data.

**LiDAR Scene Generation.** LiDAR generative models learn the distribution of point clouds and synthesize realistic scenes. Early GAN-based [1, 7, 76, 81] and VAE-based [17, 18, 31, 32, 47, 59] methods focus on object-level synthesis but fail to scale to outdoor scenes. LiDARGen [108] pioneers large-scale LiDAR generation via range-image projection and score-based modeling, while R2DM [61] and R2Flow [62] adopt diffusion models [25] for faithful synthesis. Subsequent works [28, 50, 51, 71, 86, 87, 105, 109] enhance controllability through conditional diffusion. UltraLiDAR [88] integrates voxelized LiDAR in a BEV-based VQ-VAE [82] framework for spatial compactness. For temporal modeling, ViDAR [98] predicts future LiDAR frames from historical images, while LiDARCrafter [45] employs a two-stage autoregressive framework. These methods treat spatial regions uniformly, overlooking varying semantic difficulty and uncertainty. In contrast, our work explicitly estimates and models spatial uncertainty, guiding generation in a “hard-to-easy” manner for improved structural fidelity.

**Uncertainty Modeling in 3D.** Uncertainty modeling is critical for reliable perception in safety-critical applications such as autonomous driving [3, 23]. In the image domain, prior works improve model robustness through deterministic confidence estimation [56, 74], Bayesian inference [13, 15, 24, 30], ensemble learning [22, 39, 70], test-time augmentations [4, 55], and post-hoc calibration [14, 20, 29, 64]. In the 3D domain, Zhang *et al.* [101] propose probabilistic point embeddings to enhance uncertainty estimation,

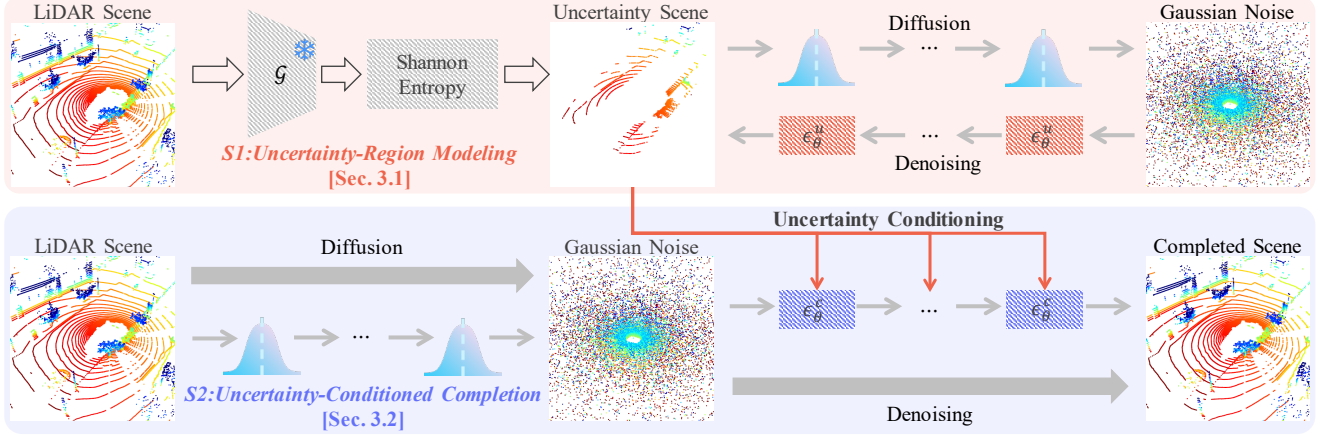


Figure 2. **Overview of the U4D framework.** U4D generates LiDAR scenes in a “hard-to-easy” manner through two stages. (1) It first estimates spatial uncertainty using a pretrained segmentation model  $\mathcal{G}$  based on Shannon Entropy, and performs an unconditional diffusion process to reconstruct high-fidelity geometry within the uncertain regions (cf. Sec. 3.1). (2) It then conducts uncertainty-conditioned completion, synthesizing the remaining scene areas guided by the reconstructed structures to ensure global consistency (cf. Sec. 3.2).

while SalsaNext [12] integrates Bayesian inference to capture epistemic and aleatoric uncertainty in LiDAR segmentation. Calib3D [35] further introduces depth-aware scaling to calibrate confidence across spatial distributions. In contrast, our work is the first to incorporate uncertainty modeling into a generative framework, explicitly leveraging estimated uncertainty regions as structural priors to guide scene synthesis and improve downstream reliability.

### 3. Methodology

We propose **U4D**, the first uncertainty-aware generative framework for LiDAR scene synthesis. As illustrated in Fig. 2, U4D generates LiDAR scenes in a “hard-to-easy” manner through two sequential stages. (1) It estimates an uncertainty map from a real scan using a pretrained segmentation model and employs an unconditional diffusion process to reconstruct high-fidelity uncertain regions (cf. Sec. 3.1). (2) Conditioned on these reconstructed areas, U4D completes the remaining scene to ensure structural integrity and global coherence (cf. Sec. 3.2). Both stages share latent representations, enabling global context to refine local uncertainty. To maintain temporal stability, U4D integrates a **Mixture of Spatio-Temporal (MoST)** block within the diffusion backbone. The MoST block decouples and adaptively fuses spatial and temporal features, enabling the generation of LiDAR sequences that are both geometrically precise and temporally coherent (cf. Sec. 3.3).

#### 3.1. Uncertainty Measurement in 3D

Real-world LiDAR scenes exhibit non-uniform difficulty across spatial regions. Some structures, such as ground or buildings, are geometrically stable and semantically consistent, while others are inherently uncertain due to factors

such as *distance-induced sparsity*, *occlusion*, *small-scale objects*, or *semantic ambiguity* between visually similar categories. These uncertainty-prone regions frequently appear at long ranges, around object boundaries, or in areas of low point density, leading to inconsistent predictions in safety-critical perception tasks. Explicitly identifying and modeling these regions allows generative models to focus first on structurally unstable and perceptually ambiguous areas before extending to the entire scene, thereby producing more realistic priors and improving downstream robustness.

**Uncertainty Maps.** To localize uncertainty regions, we derive a per-point uncertainty map from a pretrained LiDAR semantic segmentation model. Given a point cloud  $\mathcal{P}$  and a segmentation model  $\mathcal{G}$ , the model outputs per-point semantic logits  $\mathbf{Z} = \mathcal{G}(\mathcal{P}) \in \mathbb{R}^{|\mathcal{P}| \times C}$ , where  $C$  denotes the number of classes. After softmax normalization, we obtain the class probability  $D_c(\mathbf{p})$  for each point  $\mathbf{p} \in \mathcal{P}$ . The semantic uncertainty is quantified via Shannon Entropy [30, 75]:

$$H(\mathbf{p}) = - \sum_{c=1}^C D_c(\mathbf{p}) \log D_c(\mathbf{p}). \quad (1)$$

Higher entropy values correspond to greater ambiguity, typically found near class boundaries or within distant, partially occluded areas where the LiDAR returns become sparse. To maintain a consistent proportion of uncertain points across scenes, we select the top- $K$  points with the highest entropy to form a sparse uncertainty point cloud  $\mathcal{P}^u$ , which highlights geometrically or semantically uncertain regions. This point cloud serves as a structural prior for subsequent uncertainty-aware generation.

**Uncertainty-Region Representation.** To efficiently represent and model these uncertainty regions, we transform  $\mathcal{P}^u$  into a range-view format, following prior works [50,

61]. Each frame is projected onto a range image  $\mathbf{x}_0^u \in \mathbb{R}^{H \times W \times 2}$ , where each pixel encodes normalized depth and reflectance values within  $[-1, 1]$ . A binary mask  $\mathbf{m}^u \in \{0, 1\}^{H \times W \times 1}$  simultaneously indicates valid LiDAR returns in the 2D projection. This representation preserves the geometric continuity of uncertainty regions while providing dense spatial layout suitable for generative modeling.

**Uncertainty Diffusion Modeling.** To model the generative distribution of uncertainty regions, we employ an unconditional diffusion model  $\epsilon_\theta^u$  trained on the range-view representation. Following the standard denoising diffusion formulation [25], Gaussian noise is progressively added to the clean data  $\mathbf{x}_0^u$  with a predefined variance schedule  $\{\beta_t\}_{t=1}^T$ :

$$q(\mathbf{x}_t^u | \mathbf{x}_0^u) = \mathcal{N}(\mathbf{x}_t^u; \sqrt{\bar{\alpha}_t} \mathbf{x}_0^u, (1 - \bar{\alpha}_t) \mathbf{I}), \quad (2)$$

where  $\bar{\alpha}_t = \prod_{s=1}^t (1 - \beta_s)$ . During training,  $\epsilon_\theta^u$  learns to predict the injected Gaussian noise  $\epsilon^u$  while reconstructing the binary occupancy mask  $\mathbf{m}^u$  to preserve spatial validity. The training objective combines the diffusion noise prediction loss and an auxiliary mask supervision:

$$\mathcal{L}_u = \mathbb{E}_{t, \mathbf{x}_0^u, \epsilon^u} [\|\epsilon^u - \epsilon_\theta^u(\mathbf{x}_t^u, t)\|_2^2] + \lambda \mathcal{L}_{\text{mask}}(\mathbf{m}^u, \mathbf{m}^p), \quad (3)$$

where  $\mathcal{L}_{\text{mask}}$  is the binary cross-entropy loss and  $\lambda$  controls its relative weight. At inference, a Gaussian sample  $\mathbf{x}_T^u \sim \mathcal{N}(\mathbf{0}, \mathbf{I})$  is iteratively denoised to produce a structured range image  $\hat{\mathbf{x}}_0^u$  along with occupancy mask  $\mathbf{m}^p$ , which constrains generation within valid spatial regions and preserves the sparsity pattern of uncertainty scenes.

### 3.2. Uncertainty-Conditioned Scene Completion

While sparse uncertainty scenes emphasize semantically ambiguous regions or structurally unstable regions, they only capture partial geometric information. To generate complete and coherent LiDAR frames, we design an uncertainty-conditioned diffusion model that synthesizes full scenes under the guidance of these uncertainty priors.

**Problem Formulation.** Given a sparse uncertainty range image  $\mathbf{x}_0^u$ , the goal is to reconstruct a dense LiDAR observation  $\mathbf{x}_0 \in \mathbb{R}^{H \times W \times 2}$ . The conditional diffusion model  $\epsilon_\theta^c$  is trained to approximate the conditional distribution  $p(\mathbf{x}_0 | \mathbf{x}_0^u)$ , enabling the model to complete the scene while respecting the structural cues encoded in  $\mathbf{x}_0^u$ .

**Conditional Diffusion Process.** Similar to the unconditional diffusion defined in Eq. (2), the forward process gradually perturbs the complete scene  $\mathbf{x}_0$ :

$$q(\mathbf{x}_t | \mathbf{x}_0) = \mathcal{N}(\mathbf{x}_t; \sqrt{\bar{\alpha}_t} \mathbf{x}_0, (1 - \bar{\alpha}_t) \mathbf{I}). \quad (4)$$

During denoising, the model integrates uncertainty priors as conditional input:  $\epsilon_\theta^c : (\mathbf{x}_t, t, \mathbf{x}_0^u) \rightarrow \hat{\epsilon}$ . We concatenate  $\mathbf{x}_t$  and  $\mathbf{x}_0^u$  along the feature dimension, allowing the network to leverage both global and local cues from uncertainty regions to predict the denoising direction at each timestep. This

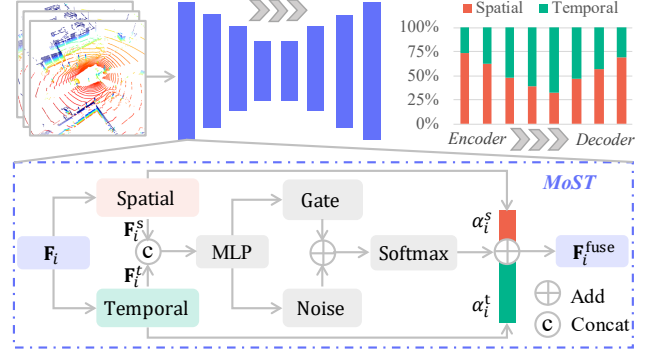


Figure 3. Illustration of the **Mixture of Spatio-Temporal (MoST)** block. It decomposes features along spatial and temporal dimensions and adaptively fuses them to maintain both spatial fidelity and temporal coherence. Near the network input and output, MoST emphasizes spatial cues, while in intermediate layers it focuses more on temporal dynamics.

explicit conditioning encourages structurally plausible and semantically consistent reconstruction.

**Training Objective.** The model is optimized with the standard conditional diffusion loss:

$$\mathcal{L}_c = \mathbb{E}_{t, \mathbf{x}_0, \epsilon^c} [\|\epsilon^c - \epsilon_\theta^c(\mathbf{x}_t, t, \mathbf{x}_0^u)\|_2^2]. \quad (5)$$

By conditioning on the uncertainty prior,  $\epsilon_\theta^c$  learns to treat these regions as structural anchors, ensuring accurate completion of occluded, distant, or small-scale objects while maintaining global scene coherence.

**Inference.** At inference, a Gaussian sample  $\mathbf{x}_T \sim \mathcal{N}(\mathbf{0}, \mathbf{I})$  is iteratively denoised conditioned on  $\hat{\mathbf{x}}_0^u$ , producing a fully reconstructed LiDAR frame  $\hat{\mathbf{x}}_0$ . The uncertainty-guided conditioning enforces spatial fidelity in challenging regions, resulting in complete scenes that are both geometrically consistent and semantically plausible.

### 3.3. Mixture of Spatio-Temporal

Temporal coherence is essential for modeling dynamic real-world environments. While prior methods [51, 61, 62] focus on spatial reconstruction, maintaining consistent temporal evolution across frames remains challenging in dynamic modeling. To jointly ensure spatial fidelity and temporal consistency, we propose the **Mixture of Spatio-Temporal (MoST)** block, as illustrated in Fig. 3. MoST is a core diffusion component that simultaneously captures fine-grained spatial geometry within each frame and smooth temporal transitions between frames, producing LiDAR sequences that are both geometrically accurate and temporally stable.

**Feature Decomposing.** Given the intermediate features  $\mathbf{F}_i \in \mathbb{R}^{C_i \times L \times H_i \times W_i}$ , where  $L$  denotes the temporal length,  $(H_i, W_i)$  represent the spatial resolutions, and  $C_i$  is the channel dimension, MoST decomposes  $\mathbf{F}_i$  into two parallel branches: a *spatial branch* that captures intra-frame geometric details through spatial convolution, producing  $\mathbf{F}_i^s$ ,



and a *temporal branch* that models inter-frame consistency via temporal convolution, yielding  $\mathbf{F}_i^t$ , with both branches having the same output shape of  $C_{i+1} \times L \times H_i \times W_i$ .

**Spatio-Temporal Adaptive Fusion.** To adaptively balance spatial and temporal cues, the two branch features are concatenated and refined through a lightweight Multi-Layer Perceptron (MLP) for shared embedding:

$$\mathbf{F}_i^{\text{share}} = \text{MLP}([\mathbf{F}_i^s; \mathbf{F}_i^t]), \quad (6)$$

where  $[\cdot; \cdot]$  denotes feature concatenation. Inspired by mixture-of-experts designs [94], we introduce a gating mechanism that dynamically adjusts the contribution of spatial and temporal activations. To enhance robustness and avoid deterministic overfitting, a stochastic noise module perturbs the gating process during training:

$$(\alpha_i^s, \alpha_i^t) = \text{Softmax}(\mathbf{F}_i^{\text{share}} \cdot \mathbf{W}_i^g + \mathbb{I}(\chi \cdot \sigma(\mathbf{F}_i^{\text{share}} \cdot \mathbf{W}_i^z))), \quad (7)$$

where  $\mathbf{W}_i^g, \mathbf{W}_i^z \in \mathbb{R}^{C_i \times 2}$  are trainable gating and noise-projection matrices,  $\chi \sim \mathcal{N}(\mathbf{0}, \mathbf{I})$  denotes Gaussian noise that stochastically perturbs feature activations,  $\sigma(\cdot)$  is the Softplus activation ensuring smooth and positive modulation, and  $\mathbb{I}(\cdot)$  activates the noise term only during training. The normalized gating weights  $(\alpha_i^s, \alpha_i^t)$  are then used to adaptively fuse the spatial and temporal features:

$$\mathbf{F}_i^{\text{fuse}} = \alpha_i^s \odot \mathbf{F}_i^s + \alpha_i^t \odot \mathbf{F}_i^t, \quad (8)$$

where  $\odot$  denotes element-wise multiplication. This adaptive fusion dynamically modulates the contributions from spatial and temporal representations, producing semantically rich and temporally consistent features.

**Weight Regularization.** To prevent the gating mechanism from overemphasizing a single modality, we introduce a regularization term encouraging balanced utilization of spatial and temporal cues:

$$\mathcal{L}_{\text{reg},i} = \frac{\text{Var}(\alpha_i^s)}{(\mathbb{E}[\alpha_i^s])^2} + \frac{\text{Var}(\alpha_i^t)}{(\mathbb{E}[\alpha_i^t])^2}, \quad (9)$$

where  $\text{Var}(\cdot)$  and  $\mathbb{E}[\cdot]$  denote variance and expectation, respectively. This term stabilizes the attention weights, ensuring MoST effectively leverages both spatial geometry and temporal dynamics without bias toward either dimension.

**Role in Our Framework.** MoST serves as a fundamental building block of the diffusion network. It simultaneously captures detailed spatial geometry within each LiDAR frame while modeling smooth temporal transitions across consecutive frames. By adaptively fusing spatial and temporal features at multiple stages of the network, MoST enables the generation of LiDAR sequences that are both geometrically precise and temporally coherent, ensuring realistic and consistent scene synthesis over time.

Table 1. **Comparison of state-of-the-art LiDAR scene generation methods** on the *nuScenes* [8] dataset. Metrics marked with  $\downarrow$  indicate that lower values are better. The **MMD** scores are reported in units of  $10^{-4}$ . The **best** and **second-best** scores are highlighted in **bold** and underline, respectively.

Method	Venue	FRD $\downarrow$	FPD $\downarrow$	JSD $\downarrow$	MMD $\downarrow$
LiDARGen [108]	ECCV'22	549.18	22.80	<u>0.04</u>	0.76
LiDM [71]	CVPR'24	-	30.77	0.07	3.86
R2DM [61]	ICRA'24	<u>253.80</u>	<u>14.35</u>	<b>0.03</b>	<b>0.48</b>
Text2LiDAR [86]	ECCV'24	953.18	147.48	0.09	12.50
UniScene [41]	CVPR'25	-	976.47	0.32	13.61
OpenDWM [63]	CVPR'25	-	714.19	0.20	5.61
<i>U4D</i>	<b>Ours</b>	<b>223.96</b>	<b>12.90</b>	<b>0.03</b>	<u>0.53</u>

## 4. Experiments

### 4.1. Configurations

**Benchmarking Details.** We conduct benchmarking experiments on the *nuScenes* [8] and *SemanticKITTI* [5] datasets, where the range image resolutions are set to  $32 \times 1024$  and  $64 \times 1024$ , respectively. All experiments are implemented using the PyTorch framework [65] on 4 NVIDIA RTX 4090 GPUs with a total batch size of 8. Following the baseline R2DM [61], the diffusion model is trained for 500,000 steps using the AdamW optimizer [54] with an initial learning rate of  $1 \times 10^{-4}$ . The learning rate follows a cosine annealing schedule with a warm-up phase during the first 10,000 steps [52]. During inference, the diffuser performs 256 denoising steps to ensure a fair comparison with the baseline R2DM [61]. Please refer to the Appendix for more details.

**Evaluation Metrics.** We assess the quality of generated LiDAR scenes from three perspectives: (1) *Geometric and Spatial Fidelity*. We adopt the **Fréchet Range Distance (FRD)**, **Fréchet Point Distance (FPD)**, **Jensen-Shannon Divergence (JSD)** and **Maximum Mean Discrepancy (MMD)** on range images, point clouds, and bird's-eye-view (BEV) [51, 61]. (2) *Temporal Coherence*. Following [45], we use the **Temporal Transformation Consistency Error (TTCE)** and **Chamfer Temporal (CTC)** metrics to measure frame-to-frame alignment accuracy and overall motion stability across sequences. (3) *Downstream Utility*. For assessing the usefulness of generated data in perception tasks, we evaluate **Mean Intersection-over-Union (mIoU)** for semantic segmentation and **Expected Calibration Error (ECE)** [35] for measuring the calibration reliability of uncertainty-aware segmentation models.

### 4.2. Comparative Study

**Scene-Level Fidelity.** We first benchmark U4D against state-of-the-art LiDAR scene generation methods from a scene-level spatial fidelity perspective. Specifically, we sample 10,000 sequences and evaluate the first frame of each sequence to ensure a fair comparison with single-frame generation baselines producing the same number of

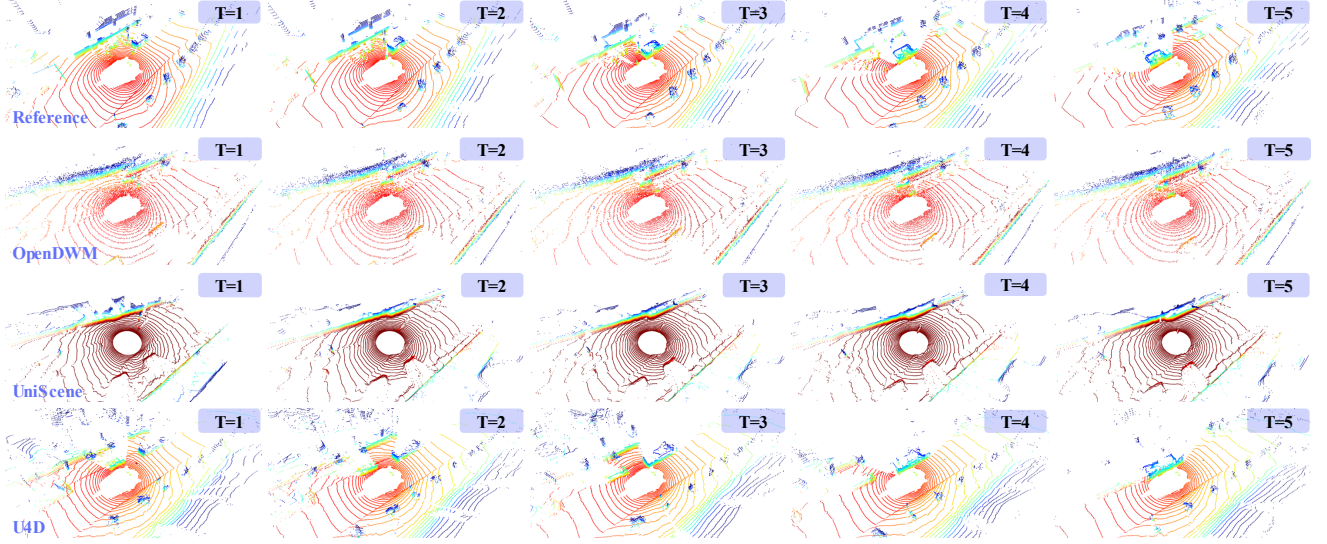


Figure 4. Qualitative results of **sequence point cloud generation** on the nuScenes dataset [8]. U4D preserves both geometric fidelity and temporal consistency, producing sequences most similar to the reference. It reliably reconstructs distant, sparse regions and captures dynamic objects across frames, maintaining coherent structure and motion. Frames are shown in temporal order from left to right. The colors are rendered based on the height information of the point cloud. Best viewed in zoom.

Table 2. **Comparison of state-of-the-art LiDAR scene generation methods** on the *SemanticKITTI* [5] dataset. Metrics marked with  $\downarrow$  indicate that lower values are better. The **MMD** scores are reported in units of  $10^{-4}$ . The **best** and **second-best** scores are highlighted in **bold** and underline, respectively.

Method	Venue	FRD $\downarrow$	FPD $\downarrow$	JSD $\downarrow$	MMD $\downarrow$
LiDARGen [108]	ECCV’22	735.49	119.69	0.13	21.90
LiDM [71]	CVPR’24	-	496.78	0.08	9.20
R2DM [61]	ICRA’24	<u>262.85</u>	<u>12.06</u>	<b>0.03</b>	<u>0.89</u>
Text2LiDAR [86]	ECCV’24	567.47	16.78	0.08	4.24
<i>U4D</i>	<b>Ours</b>	<b>245.73</b>	<b>10.92</b>	<u>0.04</u>	<b>0.85</b>

scenes. As shown in Tab. 1 and Tab. 2, U4D consistently outperforms existing methods, achieving an FRD of 223.96 and an FPD of 12.90 on nuScenes [8], and 245.73 (FRD) and 10.92 (FPD) on SemanticKITTI [5], surpassing R2DM [61] by approximately 6%-11%. For BEV-based metrics, including JSD and MMD, U4D also achieves competitive or superior performance, demonstrating robust spatial consistency across viewpoints. These results highlight U4D’s strong ability to generate geometrically accurate and perceptually consistent LiDAR scenes.

**Temporal Coherence.** Maintaining temporal coherence is crucial for sequential LiDAR generation, as inconsistent frame-to-frame predictions can lead to unrealistic scene dynamics. In Tab. 3, we evaluate U4D against recent methods, including UniScene [41], OpenDWM [63], and LiDAR-Crafter [45], on sequences sampled at 2Hz. TTCE measures deviations between predicted and ground-truth transformations via point cloud registration, while CTC computes Chamfer distances between consecutive frames. U4D

Table 3. **Comparison of temporal consistency** in 4D LiDAR scene generation on the *nuScenes* [8] dataset. Metrics marked with  $\downarrow$  indicate that lower values are better. The **best** and **second-best** scores are highlighted in **bold** and underline, respectively. Numbers denote frame intervals.

Method	Venue	TTCE $\downarrow$		CTC $\downarrow$			
		3	4	1	2	3	4
UniScene [41]	CVPR’25	2.74	3.69	<b>0.90</b>	<b>1.84</b>	3.64	<b>3.90</b>
OpenDWM [63]	CVPR’25	2.68	3.65	1.02	2.02	3.37	5.05
LiDAR-Crafter [45]	arXiv’25	<u>2.65</u>	<u>3.56</u>	1.12	2.38	<u>3.02</u>	4.81
<i>U4D</i>	<b>Ours</b>	<b>2.63</b>	<b>3.51</b>	<u>0.97</u>	<u>1.93</u>	<b>2.98</b>	<u>4.41</u>

consistently achieves the lowest TTCE scores across all frame intervals and maintains competitive CTC scores, reflecting its ability to generate temporally stable sequences with smooth and realistic motion patterns. These results highlight the effectiveness of the MoST block in capturing both spatial and temporal dependencies within sequences.

**LiDAR Semantic Segmentation.** LiDAR semantic segmentation is a fundamental perception task in autonomous driving, yet it remains highly challenging in uncertain and sparse regions. To validate the fidelity and utility of our uncertainty-aware LiDAR scene generation, we apply the generated data to downstream segmentation tasks. The overall training pipeline follows LaserMix [34], where only a subset of real data is used as labeled samples, while the remaining real data and our generated uncertainty-aware scenes are treated as unlabeled data. As shown in Tab. 4, we evaluate U4D under two popular LiDAR representations – *sparse voxels* [11] and *multi-view fusion* [79]. The results show that incorporating scenes generated by U4D consistently enhances downstream segmentation per-

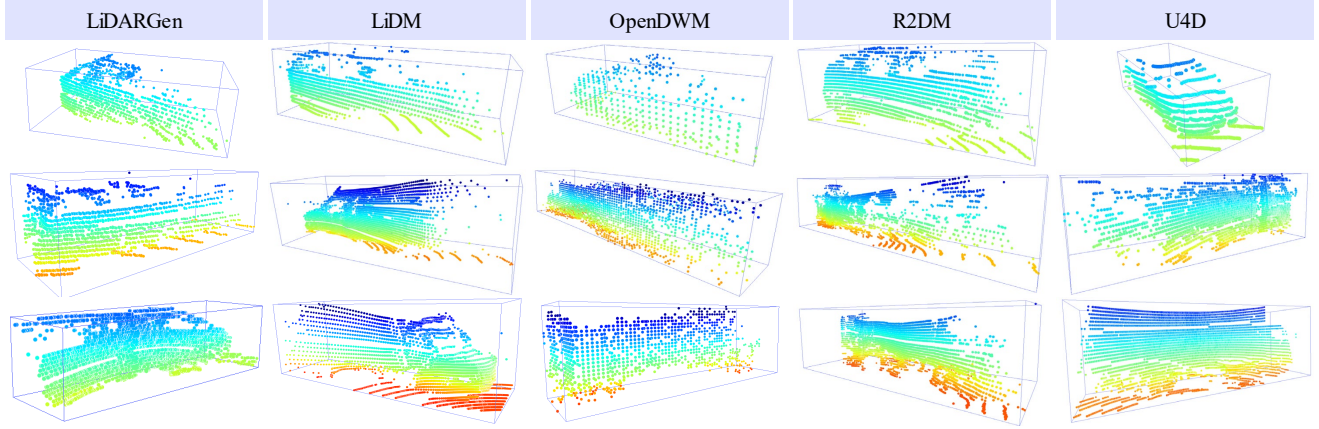


Figure 5. Qualitative results of **generated objects within scenes** on the *nuScenes* dataset [8]. U4D accurately captures object geometry and preserves fine structural details while maintaining realistic spatial relationships within the scene. From top to bottom are “car”, “bus”, and “truck” respectively. All objects are detected using a pretrained PointPillars [40] detector.

Table 4. **Comparison of state-of-the-art methods** on the downstream task of LiDAR semantic segmentation on the *val* set of the *nuScenes* [8] dataset. The voxel- and fusion-based representations are built upon MinkUNet [11] and SPVCNN [79] as backbones, respectively. The mIoU scores are reported in percentage (%). The **best** and second-best results within each data split and representation are highlighted in **bold** and underline, respectively.

Repr.	Method	Venue	nuScenes			
			1%	10%	20%	50%
Voxel	<i>Sup.-only</i>	-	58.3	71.0	73.0	75.1
	MeanTeacher [80]	NeurIPS’17	60.1	71.7	73.4	75.2
	LaserMix [34]	CVPR’23	62.8	<u>73.6</u>	<u>74.8</u>	<u>76.1</u>
	R2DM [61]	ICRA’24	<u>64.1</u>	73.0	74.3	75.9
	<b>U4D</b>	<b>Ours</b>	<b>65.3</b>	<b>73.7</b>	<b>75.0</b>	<b>76.4</b>
Fusion	<i>Sup.-only</i>	-	57.9	71.7	73.0	74.6
	MeanTeacher [80]	NeurIPS’17	59.4	72.5	73.1	74.7
	LaserMix [34]	CVPR’23	63.2	<b>74.1</b>	<u>74.6</u>	<u>75.8</u>
	R2DM [61]	ICRA’24	<u>64.6</u>	<u>72.7</u>	74.2	75.4
	<b>U4D</b>	<b>Ours</b>	<b>65.3</b>	<b>74.1</b>	<b>74.9</b>	<b>76.2</b>

Table 5. **Expected calibration error (ECE, the lower the better) of various LiDAR semantic segmentation methods** on the *validation* set of the *nuScenes* [5] and *SemanticKITTI* [5] datasets. The ECE scores are reported in percentage (%).

Method	Repr.	nuScenes		SemKITTI	
		Uncal	<b>U4D</b>	Uncal	<b>U4D</b>
RangeNet++ [58]	Range	4.57	2.72	4.01	3.31
MinkUNet [11]	Voxel	2.50	2.45	4.11	3.56
SPVCNN [79]	Fusion	2.61	2.18	3.61	3.05

formance across all label partitions, outperforming both semi-supervised learning methods [34, 80] and scene generation augmentation baselines [61]. This confirms that U4D not only generates geometrically and semantically coherent LiDAR scenes but also provides strong generalization benefits for real-world perception models.

**Uncertainty Estimation.** To quantitatively assess the bene-

fit of the proposed uncertainty-aware generation framework on real-world perception, we evaluate the calibration performance of LiDAR semantic segmentation methods using the ECE metric following Calib3D [35]. Specifically, we first generate pseudo-labels for the synthesized scenes using a pretrained segmentation model [93], and then jointly train the model with both real and generated data. As shown in Tab. 5, “Uncal” denotes models trained solely on real data. U4D consistently achieves lower ECE values, demonstrating that uncertainty-aware scene generation improves model calibration, reliability, and prediction confidence.

**Qualitative Results.** Fig. 4 presents qualitative comparisons of sequential LiDAR scenes generated by U4D and recent sequence generation methods [41, 63]. Spatially, U4D produces more realistic and structurally faithful scenes that closely match the reference. Temporally, it maintains smooth object motion and ego-motion consistency across frames. Furthermore, Fig. 5 visualizes generated object instances within scenes, where all objects are detected using a pretrained PointPillars [40] detector. As shown, U4D can generate objects with clear geometric boundaries, consistent scales, and coherent placement relative to surrounding structures. These advantages can be attributed to two factors. First, the proposed uncertainty-aware generation mechanism guides the model to focus more on ambiguous and structurally complex regions, thereby improving local geometry and object fidelity. Second, the MoST block adaptively fuses spatial and temporal cues, ensuring that objects remain temporally consistent and physically plausible throughout the generated sequence.

### 4.3. Ablation Study

**Selection of Uncertainty Regions.** Identifying suitable uncertainty regions is essential, as they provide crucial structural priors that guide the generation. In this ablation study, we evaluate different strategies for selecting uncertainty re-



Table 6. Ablation study on the **selection of uncertainty regions** on *nuScenes* [8]. Metrics marked with  $\downarrow$  indicate that lower values are better. The **MMD** scores are reported in units of  $10^{-4}$ . ECE is evaluated using RangeNet++ [58] and reported in percentage (%).

#	Metric	FRD $\downarrow$	FPD $\downarrow$	JSD $\downarrow$	MMD $\downarrow$	ECE $\downarrow$
(1)	None	235.91	14.03	0.04	0.65	3.98
(2)	Random	235.23	13.21	0.04	0.55	4.35
(3)	Confidence	228.24	13.04	<b>0.03</b>	0.72	3.02
(4)	Entropy	<b>223.96</b>	<b>12.90</b>	<b>0.03</b>	<b>0.53</b>	<b>2.72</b>

Table 7. Ablation study on the **design of the MoST block** on the *nuScenes* [8] dataset. Metrics marked with  $\downarrow$  indicate that lower values are better. The **MMD** scores are reported in units of  $10^{-4}$ .

#	Parallel	Fusion	FRD $\downarrow$	FPD $\downarrow$	JSD $\downarrow$	MMD $\downarrow$
(1)		None	536.23	23.34	0.63	2.43
(2)	$\checkmark$	Addition	242.81	13.42	0.28	0.65
(3)	$\checkmark$	Concat	242.43	<b>12.51</b>	<b>0.03</b>	0.68
(4)	$\checkmark$	Adaptively	<b>223.96</b>	<b>12.90</b>	<b>0.03</b>	<b>0.53</b>

gions, with the results summarized in Tab. 6. When trained without any uncertainty conditioning (row 1), the model achieves 235.91 FRD, 14.03 FPD, and an ECE of 3.98. Random sampling (row 2) provides negligible improvement in generation quality and even degrades calibration performance. In contrast, both confidence-based (row 3) and entropy-based (row 4) selection strategies lead to significant gains in scene fidelity and calibration, as they effectively localize regions of high semantic ambiguity. Among them, the entropy-based strategy achieves the best overall performance, demonstrating its superior ability to capture diverse and informative uncertainty patterns for guiding generation.

**Design of MoST Block.** The Mixture of Spatio-Temporal (MoST) block serves as a key component of our diffusion backbone, designed to adaptively fuse spatial and temporal cues for coherent LiDAR scene generation. In this ablation, we investigate how different fusion strategies affect generation quality, as shown in Tab. 7. We first follow prior video generation approaches [19] and apply spatial and temporal operations in a cascaded manner (row 1). This configuration yields suboptimal results, likely because the deeper cascaded structure hampers convergence and optimization. We then decompose features into spatial and temporal branches and fuse them in parallel using either element-wise addition (row 2) or concatenation (row 3). Both strategies significantly improve generation quality, as they expand network width rather than depth, facilitating more stable optimization. However, these methods treat spatial and temporal cues equally, lacking adaptive weighting. Finally, we introduce an adaptive fusion mechanism inspired by the mixture-of-experts paradigm [94] (row 4), where the model learns to dynamically balance spatial and temporal information. This design achieves the best overall generation quality, demonstrating the effectiveness of adaptive spatio-temporal fusion

Table 8. Ablation study on the **efficiency of generative models**. The table reports the average inference time per frame (**I.T.**, in seconds). “DM” refers to the diffusion model.

Method	Venue	Generator	Architecture	I.T.
LiDARGen [108]	ECCV’22	Energy-Based	U-Net	67
LiDM [71]	CVPR’24	Latent DM	Curve U-Net	3.5
R2DM [61]	ICRA’24	DM	Curve U-Net	3.5
UniScene [41]	CVPR’25	Volume Rendering	Sparse U-Net	2.1
OpenDWM [63]	CVPR’25	Latent R	U-Net	12.1
<b>U4D</b>	<b>Ours</b>	<b>DM</b>	<b>Curve U-Net</b>	<b>8.9</b>

for coherent 4D LiDAR generation.

**Spatio-Temporal Activations.** To further examine how the MoST block fuses spatial and temporal information across different network stages, we analyze the relative activation weights of its two branches. As shown in the top-right of Fig. 3, we visualize the averaged weighting distribution of spatial and temporal branches throughout the diffusion network. We observe that near the input and output layers, the spatial branch contributes more prominently, as these stages mainly focus on reconstructing local geometric details and structural integrity of LiDAR frames. In contrast, the temporal branch exhibits stronger activations in intermediate layers, where the model captures motion dynamics and ensures temporal consistency across frames. This observation validates our design intuition that spatial cues dominate at the boundaries for geometric fidelity, while temporal cues become essential in the latent space to model scene evolution and motion continuity. The adaptive allocation of activations allows MoST to balance geometric reconstruction and motion modeling, enabling the diffusion network to generate LiDAR sequences that are both spatially accurate and temporally coherent.

**Efficacy Analysis.** Tab. 8 summarizes the efficiency of U4D compared with other generative models. Compared with single-frame generators [61, 71], U4D requires slightly longer inference time since it generates multiple frames simultaneously, which inevitably increases computational demand. However, when compared to other sequential generative models, U4D demonstrates competitive efficiency while achieving superior generation quality. Its inference speed is slower than UniScene, primarily due to the higher spatial resolution of our range-based representation. These observations highlight the potential of U4D as a strong yet scalable baseline, motivating future work toward more efficient architectures such as latent diffusion models.

## 5. Conclusion

In this work, we propose **U4D**, the first uncertainty-aware generative framework for 4D LiDAR world modeling. U4D first estimates spatial uncertainty maps from a pretrained segmentation model and introduces a two-stage diffusion pipeline that generates high-fidelity LiDAR scenes in a



“hard-to-easy” manner: (1) the *uncertainty-region modeling* stage reconstructs high-entropy regions with fine geometric fidelity, and (2) the *uncertainty-conditional completion* stage synthesizes the remaining areas guided by the learned structural uncertainty prior. To further ensure temporal coherence, U4D incorporates a Mixture of Spatio-Temporal (MoST) block that adaptively modulates spatial and temporal cues, enabling geometrically precise and temporally consistent LiDAR sequences. Extensive experiments validate the effectiveness of U4D in uncertainty estimation and real-world downstream applications, paving the way toward more reliable 4D LiDAR world models.

## Appendix

<b>6. Additional Implementation Details</b>	<b>9</b>
6.1. Training Configurations	9
6.2. Evaluation Configurations	10
<b>7. Additional Qualitative Results</b>	<b>11</b>
<b>8. Broad Impact &amp; Limitations</b>	<b>11</b>
8.1. Broader Impact	12
8.2. Potential Limitations	12
<b>9. Public Resources Used</b>	<b>12</b>
9.1. Public Codebase Used	12
9.2. Public Datasets Used	12
9.3. Public Implementations Used	12

## 6. Additional Implementation Details

In this section, we provide comprehensive implementation details to facilitate reproducibility and enable understanding of our experimental setup. We elaborate on the training pipeline, network configurations, data preprocessing, and evaluation protocols adopted throughout our experiments.

### 6.1. Training Configurations

In this section, we provide detailed training configurations to facilitate the reproducibility of U4D.

**Data Preprocessing.** As described in the main paper, we first convert raw LiDAR point clouds into range-image representations, which serves as the input format for our diffusion-based generative framework. Given a 3D point  $(x_i, y_i, z_i)$ , its projected pixel coordinate  $(u_i, v_i)$  in a range image of resolution  $H \times W$  is computed as:

$$\begin{pmatrix} u_i \\ v_i \end{pmatrix} = \begin{pmatrix} \frac{1}{2} [1 - \arctan(y_i, x_i) \pi^{-1}] W \\ [1 - (\arcsin(z_i d_i^{-1}) - f_{\text{down}}) f^{-1}] H \end{pmatrix}, \quad (10)$$

where  $d_i = \sqrt{x_i^2 + y_i^2 + z_i^2}$  denotes the radial distance of the point, and  $f = f_{\text{up}} - f_{\text{down}}$  is the vertical field

of view (FOV) spanned by the LiDAR sensor. The parameters  $f_{\text{up}}$  and  $f_{\text{down}}$  correspond to the upper and lower elevation angles defined by the sensor. For range-image construction, we adopt resolutions  $(H, W) = (32, 1024)$  for nuScenes [8] and  $(64, 1024)$  for SemanticKITTI [5]. The vertical FOV settings  $(f_{\text{down}}, f_{\text{up}})$  follow the respective sensor configurations of each dataset:  $(-30^\circ, 10^\circ)$  for nuScenes [8] and  $(-25^\circ, 3^\circ)$  for SemanticKITTI [5].

Each resulting range image  $\mathbf{X} \in \mathbb{R}^{H \times W \times 2}$  contains two channels – depth and intensity<sup>1</sup>. To stabilize diffusion training, we apply depth compression and channel-level normalization before feeding data to the model. For the depth channel, we employ a logarithmic compression [61]:

$$\mathbf{X}_d^{\text{norm}} = \frac{\log_2(\mathbf{X}_d + 1)}{\log_2(d_{\text{max}} + 1)}, \quad (11)$$

where  $d_{\text{max}}$  is the maximum measurable LiDAR range, set to 80.0 meters in all experiments. This compression mitigates the large dynamic range of raw depth value and enhances the stability of diffusion noise prediction, particularly in distant sparse regions. Then, all pixel values are linearly scaled into the range  $[-1, 1]$  as:

$$\mathbf{X}^{\text{input}} = 2 \cdot \mathbf{X}^{\text{norm}} - 1. \quad (12)$$

This standardization step ensures consistent input statistics across datasets and improves training convergence.

**Network Architectures.** Following R2DM [61], we adopt a 4-layer Efficient U-Net [72] as the backbone of our diffusion network, with intermediate feature dimensions of 64, 128, 256, and 512. Each layer contains three Mixture of Spatio-Temporal (MoST) blocks, and the spatial resolution is downsampled by a factor of two along both the vertical and horizontal dimensions in the last three layers. In a MoST block, the input features are denoted as  $\mathbf{F}_i \in \mathbb{R}^{C_i \times L \times H_i \times W_i}$ , where  $C_i$  is the channel dimension,  $L$  is the temporal length, and  $(H_i, W_i)$  are the spatial resolutions at the  $i$ -th layer. The spatial branch processes  $\mathbf{F}_i$  using a  $1 \times 3 \times 3$  convolution to encode intra-frame geometric structures, while the temporal branch applies a  $3 \times 1 \times 1$  convolution to capture inter-frame temporal dependencies. The outputs of the two branches are fused and added back to the input through a residual connection, ensuring stable training and efficient integration of spatial and temporal cues throughout the diffusion process.

**Selection of Uncertainty Regions.** To determine the uncertainty regions, we employ a pretrained RangeNet++ [58] semantic segmentation model to estimate the per-pixel class probability distribution. For each point, we compute its Shannon Entropy [75] as:

$$H(\mathbf{p}) = \sum_{c=1}^C D(c | \mathbf{p}) \log D(c | \mathbf{p}), \quad (13)$$

<sup>1</sup>For the nuScenes [8] dataset, the raw intensity values lies in  $[0, 255]$  and are normalized to  $[0, 1]$  by dividing by 255.0.

where  $D(c | \mathbf{p})$  denotes the predicted probability of class  $c$  for point  $\mathbf{p}$ , and  $C$  is the total number of semantic classes. Points with higher entropy represent regions with greater semantic ambiguity, typically corresponding to object boundaries, distant structures, or sparsely scanned areas. To ensure sparse yet consistent uncertainty-mask coverage across the dataset, we retain the top-20% highest-entropy points for nuScenes [8] and the top-5% for SemanticKITTI [5]. These ratios are chosen to provide sufficient supervisory signal for ambiguous regions while preserving stable coverage across frames and sequences.

**Training Hyperparameters.** We employ a two-stage training pipeline for U4D using the PyTorch [65] framework. The first stage, *uncertainty-region modeling*, is trained for 1,000,000 steps, whereas the second stage, *uncertainty-conditioned completion*, is trained for 500,000 steps. Both stages use a batch size of 8 with a sequence length of 6. We use the AdamW optimizer [54] with a learning rate of  $1 \times 10^{-4}$ ,  $\beta_1 = 0.9$ ,  $\beta_2 = 0.99$ , and  $\epsilon = 1 \times 10^{-8}$ . The learning rate follows a cosine annealing schedule with a warm-up period of the first 10,000 steps [52]. To further stabilize optimization, we apply an exponential moving average (EMA) with a decay rate of 0.995, updated every 10 training steps. The diffusion process adopts continuous timesteps with a cosine noise schedule, consistent with R2DM [61]. During inference, we use 256 sampling steps to ensure a fair comparison with R2DM [61]. All experiments are conducted on a server equipped with four NVIDIA RTX 4090 GPUs under mixed-precision (FP16) training.

## 6.2. Evaluation Configurations

This section summarizes the evaluation configurations and metrics used to assess the quality of LiDAR scene generation from three perspectives: <sup>1</sup>*Geometric and Spatial Fidelity*, <sup>2</sup>*Temporal Coherence*, and <sup>3</sup>*Downstream Utility*.

**Geometric and Spatial Fidelity.** This set of metrics evaluates how accurately the generated LiDAR scenes capture the geometry and spatial structure of real-world environments. We adopt four measures:

*Fréchet Range Distance (FRD).* FRD quantitatively evaluates the generation quality in the range image domain, which provides a structured 2D representation of LiDAR point clouds. Given the real set  $\mathcal{R}$  and the generated set  $\mathcal{G}$ , their corresponding range images are processed using a RangeNet++ [58] model pretrained for semantic segmentation on the real dataset. The intermediate feature activations extracted from the backbone are denoted as  $\mathcal{F}_r$  and  $\mathcal{F}_g$ , representing the feature distributions of real and generated scenes, respectively. The FRD is computed as:

$$\text{FRD}(\mathcal{R}, \mathcal{G}) = \|\mu_g - \mu_r\|_2^2 + \text{Tr} \left( \Sigma_g + \Sigma_r - 2(\Sigma_g \Sigma_r)^{\frac{1}{2}} \right), \quad (14)$$

where  $\mu_r$  and  $\mu_g$  denote the mean feature embeddings of  $\mathcal{F}_r$  and  $\mathcal{F}_g$ ,  $\Sigma_r$  and  $\Sigma_g$  represent their corresponding covariance matrices, and  $\text{Tr}(\cdot)$  denotes the matrix trace. A lower FRD value indicates that the generated samples more closely match real LiDAR scenes in the learned feature space, implying higher fidelity and semantic consistency.

*Fréchet Point Distance (FPD).* While FRD operates in the range image domain, FPD assesses the generation quality directly in the 3D point cloud space, offering a complementary geometric perspective. Following [61], we employ a PointNet [67] model pretrained on the ShapeNet dataset [9] for 16-class object classification to extract high-level geometric features from both the real and generated point clouds, resulting in feature sets  $\mathcal{F}_r^p$  and  $\mathcal{F}_g^p$ . Analogous to FRD, the FPD is formulated as:

$$\text{FPD}(\mathcal{R}, \mathcal{G}) = \|\mu_g^p - \mu_r^p\|_2^2 + \text{Tr} \left( \Sigma_g^p + \Sigma_r^p - 2(\Sigma_g^p \Sigma_r^p)^{\frac{1}{2}} \right), \quad (15)$$

where  $\mu_r^p$  and  $\mu_g^p$  denote the mean feature embeddings of  $\mathcal{F}_r^p$  and  $\mathcal{F}_g^p$ , and  $\Sigma_r^p$  and  $\Sigma_g^p$  are their corresponding covariance matrices. A smaller FPD score suggests that the generated point distributions closely resemble those of the real-world LiDAR data in the latent geometric space, capturing fine-grained structural details beyond surface-level similarities.

*Jensen-Shannon Divergence (JSD).* JSD measures the similarity between the spatial occupancy distributions of real and generated LiDAR scenes from the bird’s-eye-view (BEV) perspective. For each sample, we compute a 2D occupancy histogram projected onto the BEV plane, resulting in two probability distributions, denoted as  $P$  (real) and  $Q$  (generated). The JSD is then defined as:

$$\text{JSD}(P||Q) = \frac{\text{KL}(P||M)}{2} + \frac{\text{KL}(Q||M)}{2}, \quad (16)$$

where  $M = (P + Q)/2$  and  $\text{KL}(\cdot||\cdot)$  denotes the Kullback-Leibler divergence. A lower JSD value indicates that the generated BEV occupancy maps better approximate the global spatial distribution of real scenes.

*Maximum Mean Discrepancy (MMD).* MMD also evaluates distributional similarity in the BEV domain, but from a kernel-based perspective. Given the same occupancy histograms  $P$  and  $Q$ , MMD is defined as:

$$\text{MMD}(P, Q) = \|\mathbb{E}_P[\phi(x)] - \mathbb{E}_Q[\phi(y)]\|_{\mathcal{H}}^2. \quad (17)$$

where  $\phi(\cdot)$  denotes the feature mapping to a reproducing kernel Hilbert space (RKHS). A smaller MMD value reflects a higher degree of alignment between the real and generated distributions, complementing JSD by providing a non-parametric statistical measure.

**Temporal Coherence.** Temporal coherence measures how consistently the generated LiDAR scenes evolve over time, ensuring smooth object motion and realistic scene dynamics. Following [45], we adopt two metrics:

*Temporal Transformation Consistency Error (TTCE).* TTCE evaluates the temporal coherence of generated LiDAR sequences by comparing frame-to-frame transformations against ground truth. We first apply the Iterative Closest Point (ICP) algorithm [6] to consecutive generated frames to estimate the rigid transformation  $\mathbf{T}^p = [\mathbf{R}^p \mid \mathbf{t}^p]$ , where  $\mathbf{R}^p$  and  $\mathbf{t}^p$  denote rotation and translation, respectively. Let  $\mathbf{T}^g = [\mathbf{R}^g \mid \mathbf{t}^g]$  be the ground-truth transformation. TTCE is computed as:

$$\text{TTCE}_{\text{rot}} = \frac{1}{T-1} \sum_{t=1}^{T-1} \|\mathbf{R}_t^p(\mathbf{R}_t^g) - \mathbf{I}\|_F, \quad (18)$$

$$\text{TTCE}_{\text{trans}} = \frac{1}{T-1} \sum_{t=1}^{T-1} \|\mathbf{t}_t^p - \mathbf{t}_t^g\|_2, \quad (19)$$

where  $T$  is the number of frames and  $\|\cdot\|_F$  denotes the Frobenius norm. Lower TTCE values indicate better alignment with the ground-truth transformations, reflecting higher temporal consistency and more realistic motion in the generated LiDAR sequences.

*Chamfer Temporal Consistency (CTC).* CTC measures temporal smoothness at the geometric level by computing the Chamfer Distance (CD) between consecutive frames after aligning them using ground-truth transformations. Let  $\mathcal{P}_t$  and  $\mathcal{P}_{t+1}$  be generated point clouds at frames  $t$  and  $t+1$ . We align  $\mathcal{P}_{t+1}$  to frame  $t$  via:

$$\hat{\mathcal{P}}_{t+1} = (\mathbf{R}_t^g)^{-1}(\mathcal{P}_{t+1} - \mathbf{t}_t^g). \quad (20)$$

The Chamfer Distance between  $\mathcal{P}_t$  and  $\hat{\mathcal{P}}_{t+1}$  is:

$$\begin{aligned} \text{CD}(\mathcal{P}_t, \hat{\mathcal{P}}_{t+1}) = & \frac{1}{|\mathcal{P}_t|} \sum_{x \in \mathcal{P}_t} \min_{y \in \hat{\mathcal{P}}_{t+1}} \|x - y\|_2^2 + \\ & \frac{1}{|\hat{\mathcal{P}}_{t+1}|} \sum_{y \in \hat{\mathcal{P}}_{t+1}} \min_{x \in \mathcal{P}_t} \|y - x\|_2^2. \end{aligned} \quad (21)$$

CTC is then averaged across all consecutive frame pairs:

$$\text{CTC} = \frac{1}{T-1} \sum_{t=1}^{T-1} \text{CD}(\mathcal{P}_t, \hat{\mathcal{P}}_{t+1}). \quad (22)$$

Lower CTC values indicate smoother frame-to-frame transitions, reflecting stronger temporal coherence in the generated 4D LiDAR sequences.

**Downstream Utility.** To evaluate the practical usefulness of generated LiDAR sequences for real-world perception tasks, we consider two downstream metrics: semantic segmentation performance and model calibration.

*Mean Intersection-over-Union (mIoU).* mIoU is a standard evaluation metric for semantic segmentation that quantifies the overlap between predicted and ground-truth regions over all classes. It is computed as:

$$\text{mIoU} = \frac{1}{|\mathbb{C}|} \sum_{c \in \mathbb{C}} \frac{\text{TP}_c}{\text{TP}_c + \text{FP}_c + \text{FN}_c}, \quad (23)$$

where  $\mathbb{C}$  denotes the set of semantic classes, and  $\text{TP}_c$ ,  $\text{FP}_c$ , and  $\text{FN}_c$  represent the number of true positives, false positives, and false negatives for class  $c$ , respectively. Higher mIoU values indicate more accurate segmentation and better utilization of generated LiDAR scenes in downstream perception tasks.

*Expected Calibration Error (ECE).* ECE is an important metric that evaluates the calibration of a perception model, i.e., how well the predicted confidence aligns with the actual accuracy. It is defined as:

$$\text{ECE} = \frac{1}{M} \sum_{m=1}^M \frac{|B_m|}{N} |\text{acc}(B_m) - \text{conf}(B_m)|, \quad (24)$$

where  $M$  is the number of confidence bins,  $N$  is the total number of samples, and  $|B_m|$  is the number of samples falling into the  $m$ -th bin.  $\text{acc}(B_m)$  and  $\text{conf}(B_m)$  denote the empirical accuracy and average confidence of bin  $B_m$ , respectively. Lower ECE values indicate better calibration, meaning the model's predicted probabilities closely match the true likelihood of correctness, which is particularly important for evaluating uncertainty-aware modeling.

## 7. Additional Qualitative Results

In Fig. 6, we present qualitative comparisons between U4D and a recent state-of-the-art LiDAR sequence generator [63], together with the corresponding reference sequences. U4D exhibits notably improved geometric fidelity and temporal coherence. It better preserves fine-grained structures that are often blurred or missing in prior methods, and in distant or low-density regions it reconstructs plausible planar surfaces with correct depth gradients. This robustness benefits from the proposed uncertainty-region modeling, which directs generation capacity toward hard-to-reconstruct areas. For dynamic objects, U4D yields smoother inter-frame transitions and more consistent object shapes and trajectories. The MoST block plays a key role here by enhancing temporal activations in intermediate layers while preserving spatial details elsewhere, enabling a more balanced spatio-temporal representation.

Beyond reconstructing observed sequences, we also explore U4D's capability for future frame prediction. As shown in Fig. 7, given only the first frame, U4D can generate plausible future LiDAR observations that exhibit coherent scene evolution and realistic motion patterns. This highlights the model's ability not only to replicate existing sequences but also to forecast future dynamics in a physically consistent manner.

## 8. Broad Impact & Limitations

In this section, we discuss the broader impact of U4D and outline its potential limitations to provide a balanced and transparent assessment of our work.

## 8.1. Broader Impact

U4D contributes to the development of safer and more scalable autonomous driving systems by enabling high-fidelity LiDAR scene generation at both spatial and temporal levels. Its capability to synthesize realistic 4D LiDAR sequences can substantially reduce the cost of data collection and annotation, particularly for safety-critical or rare scenarios such as adverse weather, long-tail object categories, and hazardous corner cases. This can accelerate the training and benchmarking of perception models, facilitate research in uncertainty estimation, and alleviate the heavy dependency on real-world data collection, which often poses privacy, safety, and logistical challenges.

Moreover, U4D can support simulation platforms and digital-twin systems by offering controllable, diverse, and uncertainty-aware scene generation. These synthetic environments can improve reproducibility, broaden research access, and lower the entry barrier for institutions with limited resources, thereby fostering a more inclusive and equitable autonomous driving research ecosystem.

Nonetheless, as with other generative frameworks, misuse is possible. Synthetic LiDAR data could, in principle, be used to create deceptive or manipulated sensor recordings. We therefore encourage responsible and transparent use of generative models and recommend deploying proper verification and auditing mechanisms to mitigate unintended or malicious misuse.

## 8.2. Potential Limitations

Despite the strong performance of U4D, several limitations remain and point toward directions for future improvement. **Scene Diversity and Rare Case Modeling.** The generative capability of U4D is inherently tied to the data distribution it is trained on. While it performs robustly on common driving scenes, it may struggle to accurately reproduce extremely rare events or highly complex environments that are sparsely represented in the training set. Capturing such tail scenarios may require more diverse datasets or the integration of additional priors.

**Computational Cost.** Although U4D adopts an efficient architecture, generating long-range temporally consistent 4D LiDAR sequences remains computationally expensive. The two-stage diffusion process requires considerable GPU resources for training, and real-time generation is still challenging for large-scale or on-vehicle deployment.

**Limited Generation Horizon.** While U4D excels at modeling short-term temporal dynamics, its performance degrades when generating sequences longer than approximately 10 frames. This limitation mainly arises from the accumulation of stochastic errors during iterative denoising, which becomes more pronounced in the range-image space where generation is performed in a pixel-level manner. Small inconsistencies in the latent features can be am-

plified during decoding back into point clouds, leading to geometric drift, motion inconsistency, or structural artifacts over longer horizons. Developing more stable latent representations, stronger temporal constraints, or hierarchical generation strategies could alleviate this limitation.

## 9. Public Resources Used

In this section, we acknowledge the use of the following public resources, during the course of this work.

### 9.1. Public Codebase Used

We acknowledge the use of the following public codebase, during the course of this work:

- MMEngine<sup>2</sup> ..... Apache License 2.0
- MMCV<sup>3</sup> ..... Apache License 2.0
- MMDetection<sup>4</sup> ..... Apache License 2.0
- MMDetection3D<sup>5</sup> ..... Apache License 2.0
- OpenPCDet<sup>6</sup> ..... Apache License 2.0

### 9.2. Public Datasets Used

We acknowledge the use of the following public datasets, during the course of this work:

- nuScenes<sup>7</sup> ..... CC BY-NC-SA 4.0
- SemanticKITTI<sup>8</sup> ..... CC BY-NC-SA 4.0

### 9.3. Public Implementations Used

We acknowledge the use of the following implementations, during the course of this work:

- pytorch<sup>9</sup> ..... BSD License
- nuscenes-devkit<sup>10</sup> ..... Apache License 2.0
- r2dm<sup>11</sup> ..... MIT License
- lidarcrater<sup>12</sup> ..... MIT License
- Open3D<sup>13</sup> ..... MIT License
- torchsparse<sup>14</sup> ..... MIT License
- LiMoE<sup>15</sup> ..... Apache License 2.0
- Vista<sup>16</sup> ..... Apache License 2.0

<sup>2</sup><https://github.com/open-mmlab/mengine>.

<sup>3</sup><https://github.com/open-mmlab/mmcv>.

<sup>4</sup><https://github.com/open-mmlab/mmdetection>.

<sup>5</sup><https://github.com/open-mmlab/mmdetection3d>.

<sup>6</sup><https://github.com/open-mmlab/OpenPCDet>.

<sup>7</sup><https://www.nuscenes.org/nuscenes>.

<sup>8</sup><https://semantic-kitti.org>.

<sup>9</sup><https://github.com/pytorch/pytorch>.

<sup>10</sup><https://github.com/nutonomy/nuscenes-devkit>.

<sup>11</sup><https://github.com/kazuto1011/r2dm>.

<sup>12</sup><https://github.com/worldbench/lidarcrater>.

<sup>13</sup><https://github.com/isl-org/Open3D>.

<sup>14</sup><https://github.com/mit-han-lab/torchsparse>.

<sup>15</sup><https://github.com/Xiangxu-0103/LiMoE>.

<sup>16</sup><https://github.com/OpenDriveLab/Vista>.



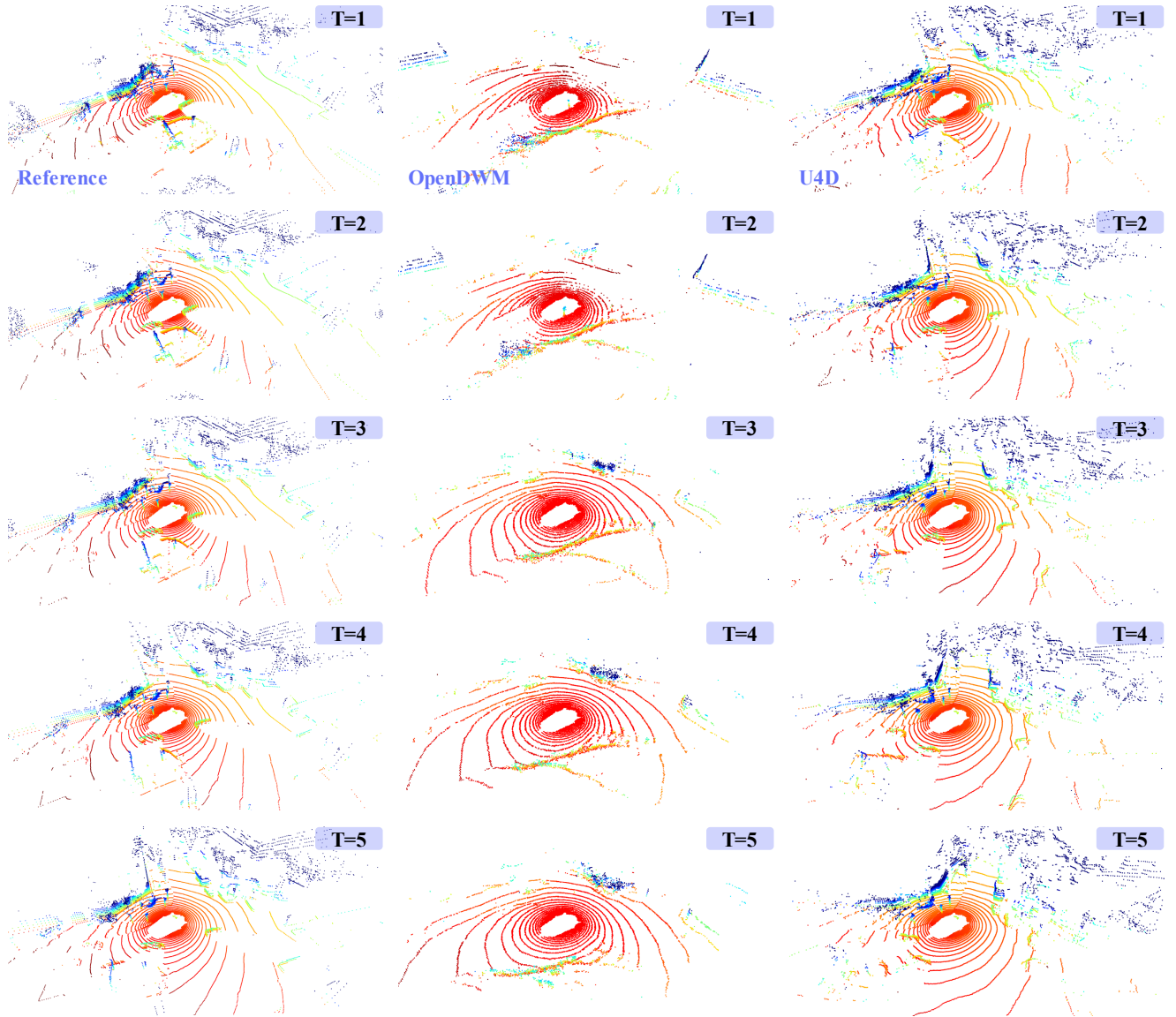


Figure 6. Qualitative results of **sequence point cloud generation** on the nuScenes dataset [8]. U4D preserves both geometric fidelity and temporal consistency, producing sequences most similar to the reference. It reliably reconstructs distant, sparse regions and captures dynamic objects across frames, maintaining coherent structure and motion. Frames are shown in temporal order from top to bottom. The colors are rendered based on the height information of the point cloud. Best viewed in zoom.

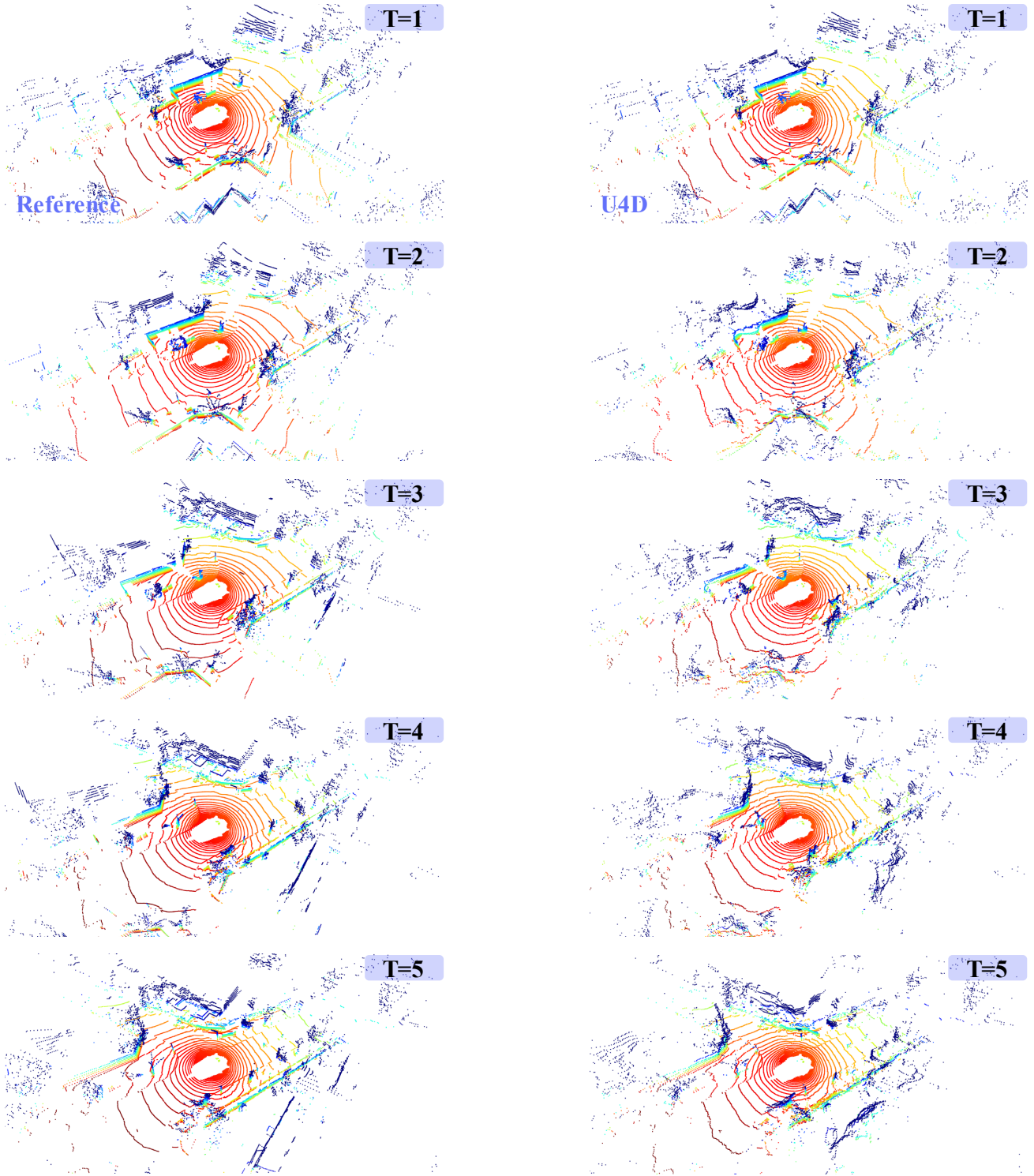


Figure 7. **Future scene prediction** on the nuScenes dataset [8]. Given only the first frame as input, U4D can predict plausible future LiDAR frames that maintain both geometric fidelity and temporal consistency. The model successfully captures object motion, scene evolution, and structural continuity across time. Frames are shown in temporal order from top to bottom. The colors are rendered based on the height information of the point cloud. Best viewed in zoom.

## References

- [1] Panos Achlioptas, Olga Diamanti, Ioannis Mitliagkas, and Leonidas Guibas. Learning representations and generative models for 3D point clouds. In *International Conference on Machine Learning*, pages 40–49, 2018. 2
- [2] Angelika Ando, Spyros Gidaris, Andrei Bursuc, Gilles Puy, Alexandre Boulch, and Renaud Marlet. RangeViT: Towards vision transformers for 3D semantic segmentation in autonomous driving. In *IEEE/CVF Conference on Computer Vision and Pattern Recognition*, pages 5240–5250, 2023. 2
- [3] Arsenii Ashukha, Alexander Lyzhov, Dmitry Molchanov, and Dmitry Vetrov. Pitfalls of in-domain uncertainty estimation and ensembling in deep learning. *arXiv preprint arXiv:2002.06470*, 2020. 2
- [4] Murat Seckin Ayhan and Philipp Berens. Test-time data augmentation for estimation of heteroscedastic aleatoric uncertainty in deep neural networks. In *Medical Imaging with Deep Learning*, 2018. 2
- [5] Jens Behley, Martin Garbade, Andres Milioto, Jan Quenzel, Sven Behnke, Cyrill Stachniss, and Jurgen Gall. SemanticKITTI: A dataset for semantic scene understanding of LiDAR sequences. In *IEEE/CVF International Conference on Computer Vision*, pages 9297–9307, 2019. 2, 5, 6, 7, 9, 10
- [6] Paul J Besl and Neil D McKay. Method for registration of 3-D shapes. In *Sensor Fusion IV: Control Paradigms and Data Structures*, pages 586–606, 1992. 11
- [7] Lucas Caccia, Herke Van Hoof, Aaron Courville, and Joelle Pineau. Deep generative modeling of LiDAR data. In *IEEE/RSJ International Conference on Intelligent Robots and Systems*, pages 5034–5040, 2019. 2
- [8] Holger Caesar, Varun Bankiti, Alex H Lang, Sourabh Vora, Venice Erin Liong, Qiang Xu, Anush Krishnan, Yu Pan, Giancarlo Baldan, and Oscar Beijbom. nuScenes: A multi-modal dataset for autonomous driving. In *IEEE/CVF Conference on Computer Vision and Pattern Recognition*, pages 11621–11631, 2020. 2, 5, 6, 7, 8, 9, 10, 13, 14
- [9] Angel X Chang, Thomas Funkhouser, Leonidas Guibas, Pat Hanrahan, Qixing Huang, Zimo Li, Silvio Savarese, Manolis Savva, Shuran Song, Hao Su, et al. ShapeNet: An information-rich 3D model repository. *arXiv preprint arXiv:1512.03012*, 2015. 10
- [10] Qi Chen, Sourabh Vora, and Oscar Beijbom. PolarStream: Streaming object detection and segmentation with polar pillars. In *Advances in Neural Information Processing Systems*, pages 26871–26883, 2021. 2
- [11] Christopher Choy, JunYoung Gwak, and Silvio Savarese. 4D spatio-temporal convnets: Minkowski convolutional neural networks. In *IEEE/CVF Conference on Computer Vision and Pattern Recognition*, pages 3075–3084, 2019. 2, 6, 7
- [12] Tiago Cortinhal, George Tzelepis, and Eren Erdal Aksoy. Salsanext: Fast, uncertainty-aware semantic segmentation of lidar point clouds for autonomous driving. In *International Symposium on Visual Computing*, pages 207–222, 2020. 3
- [13] John Denker and Yann LeCun. Transforming neural-net output levels to probability distributions. In *Advances in Neural Information Processing Systems*, 1990. 2
- [14] Zhipeng Ding, Xu Han, Peirong Liu, and Marc Niethammer. Local temperature scaling for probability calibration. In *IEEE/CVF International Conference on Computer Vision*, pages 6889–6899, 2021. 2
- [15] Yarin Gal and Zoubin Ghahramani. Dropout as a bayesian approximation: Representing model uncertainty in deep learning. In *International Conference on Machine Learning*, pages 1050–1059, 2016. 2
- [16] Biao Gao, Yancheng Pan, Chengkun Li, Sibao Geng, and Huijing Zhao. Are we hungry for 3D LiDAR data for semantic segmentation? a survey of datasets and methods. *IEEE Transactions on Intelligent Transportation Systems*, 23(7):6063–6081, 2021. 1
- [17] Lin Gao, Jie Yang, Tong Wu, Yu-Jie Yuan, Hongbo Fu, Yu-Kun Lai, and Hao Zhang. SDM-NET: Deep generative network for structured deformable mesh. *ACM Transactions on Graphics*, 38(6):1–15, 2019. 2
- [18] Lin Gao, Tong Wu, Yu-Jie Yuan, Ming-Xian Lin, Yu-Kun Lai, and Hao Zhang. TM-NET: Deep generative networks for textured meshes. *ACM Transactions on Graphics*, 40(6):1–15, 2021. 2
- [19] Shenyuan Gao, Jiazhi Yang, Li Chen, Kashyap Chitta, Yihang Qiu, Andreas Geiger, Jun Zhang, and Hongyang Li. Vista: A generalizable driving world model with high fidelity and versatile controllability. In *Advances in Neural Information Processing Systems*, pages 91560–91596, 2024. 8
- [20] Chuan Guo, Geoff Pleiss, Yu Sun, and Kilian Q Weinberger. On calibration of modern neural networks. In *International Conference on Machine Learning*, pages 1321–1330, 2017. 2
- [21] Yulan Guo, Hanyun Wang, Qingyong Hu, Hao Liu, Li Liu, and Mohammed Bennamoun. Deep learning for 3D point clouds: A survey. *IEEE Transactions on Pattern Analysis and Machine Intelligence*, 43(12):4338–4364, 2020. 1
- [22] Fredrik K Gustafsson, Martin Danelljan, and Thomas B Schon. Evaluating scalable bayesian deep learning methods for robust computer vision. In *IEEE/CVF Conference on Computer Vision and Pattern Recognition Workshops*, pages 318–319, 2020. 2
- [23] Dan Hendrycks and Kevin Gimpel. A baseline for detecting misclassified and out-of-distribution examples in neural networks. *arXiv preprint arXiv:1610.02136*, 2016. 2
- [24] Jose Hernandez-Lobato, Yingzhen Li, Mark Rowland, Thang Bui, Daniel Hernández-Lobato, and Richard Turner. Black-box alpha divergence minimization. In *International Conference on Machine Learning*, pages 1511–1520, 2016. 2
- [25] Jonathan Ho, Ajay Jain, and Pieter Abbeel. Denoising diffusion probabilistic models. In *Advances in Neural Information Processing Systems*, pages 6840–6851, 2020. 2, 4
- [26] Fangzhou Hong, Hui Zhou, Xinge Zhu, Hongsheng Li, and Ziwei Liu. LiDAR-based panoptic segmentation via dynamic shifting network. In *IEEE/CVF Conference on Com-*

- puter Vision and Pattern Recognition, pages 13090–13099, 2021. 2
- [27] Qingyong Hu, Bo Yang, Linhai Xie, Stefano Rosa, Yulan Guo, Zhihua Wang, Niki Trigoni, and Andrew Markham. RandLA-Net: Efficient semantic segmentation of large-scale point clouds. In *IEEE/CVF Conference on Computer Vision and Pattern Recognition*, pages 11108–11117, 2020. 2
- [28] Qianjiang Hu, Zhimin Zhang, and Wei Hu. RangeLDM: Fast realistic LiDAR point cloud generation. In *European Conference on Computer Vision*, pages 115–135, 2024. 2
- [29] Elias Kassapis, Georgi Dikov, Deepak K Gupta, and Cedric Nugteren. Calibrated adversarial refinement for stochastic semantic segmentation. In *IEEE/CVF International Conference on Computer Vision*, pages 7057–7067, 2021. 2
- [30] Alex Kendall and Yarin Gal. What uncertainties do we need in bayesian deep learning for computer vision? In *Advances in Neural Information Processing Systems*, 2017. 2, 3
- [31] Jinwoo Kim, Jaehoon Yoo, Juho Lee, and Seunghoon Hong. SetVAE: Learning hierarchical composition for generative modeling of set-structured data. In *IEEE/CVF Conference on Computer Vision and Pattern Recognition*, pages 15059–15068, 2021. 2
- [32] Roman Klokov, Edmond Boyer, and Jakob Verbeek. Discrete point flow networks for efficient point cloud generation. In *European Conference on Computer Vision*, pages 694–710, 2020. 2
- [33] Lingdong Kong, Youquan Liu, Runnan Chen, Yuexin Ma, Xinge Zhu, Yikang Li, Yuenan Hou, Yu Qiao, and Ziwei Liu. Rethinking range view representation for LiDAR segmentation. In *IEEE/CVF International Conference on Computer Vision*, pages 228–240, 2023. 2
- [34] Lingdong Kong, Jiawei Ren, Liang Pan, and Ziwei Liu. LaserMix for semi-supervised LiDAR semantic segmentation. In *IEEE/CVF Conference on Computer Vision and Pattern Recognition*, pages 21705–21715, 2023. 6, 7
- [35] Lingdong Kong, Xiang Xu, Jun Cen, Wenwei Zhang, Liang Pan, Kai Chen, and Ziwei Liu. Calib3D: Calibrating model preferences for reliable 3D scene understanding. In *IEEE/CVF Winter Conference on Applications of Computer Vision*, pages 1965–1978. IEEE, 2025. 3, 5, 7
- [36] Lingdong Kong, Xiang Xu, Youquan Liu, Jun Cen, Runnan Chen, Wenwei Zhang, Liang Pan, Kai Chen, and Ziwei Liu. LargeAD: Large-scale cross-sensor data pretraining for autonomous driving. *IEEE Transactions on Pattern Analysis and Machine Intelligence*, 2025. 1
- [37] Lingdong Kong, Xiang Xu, Jiawei Ren, Wenwei Zhang, Liang Pan, Kai Chen, Wei Tsang Ooi, and Ziwei Liu. Multi-modal data-efficient 3D scene understanding for autonomous driving. *IEEE Transactions on Pattern Analysis and Machine Intelligence*, 47(5):3748–3765, 2025. 2
- [38] Lingdong Kong, Wesley Yang, Jianbiao Mei, Youquan Liu, Ao Liang, Dekai Zhu, Dongyue Lu, Wei Yin, Xiaotao Hu, Mingkai Jia, et al. 3D and 4D world modeling: A survey. *arXiv preprint arXiv:2509.07996*, 2025. 1
- [39] Balaji Lakshminarayanan, Alexander Pritzel, and Charles Blundell. Simple and scalable predictive uncertainty estimation using deep ensembles. In *Advances in Neural Information Processing Systems*, 2017. 2
- [40] Alex H Lang, Sourabh Vora, Holger Caesar, Lubing Zhou, Jiong Yang, and Oscar Beijbom. PointPillars: Fast encoders for object detection from point clouds. In *IEEE/CVF Conference on Computer Vision and Pattern Recognition*, pages 12697–12705, 2019. 7
- [41] Bohan Li, Jiazhe Guo, Hongsi Liu, Yingshuang Zou, Yikang Ding, Xiwu Chen, Hu Zhu, Feiyang Tan, Chi Zhang, Tiancai Wang, et al. UniScene: Unified occupancy-centric driving scene generation. In *Proceedings of the Computer Vision and Pattern Recognition Conference*, pages 11971–11981, 2025. 5, 6, 7, 8
- [42] Li Li, Hubert PH Shum, and Toby P Breckon. Less is more: Reducing task and model complexity for 3D point cloud semantic segmentation. In *IEEE/CVF Conference on Computer Vision and Pattern Recognition*, pages 9361–9371, 2023. 2
- [43] Ying Li, Lingfei Ma, Zilong Zhong, Fei Liu, Michael A Chapman, Dongpu Cao, and Jonathan Li. Deep learning for LiDAR point clouds in autonomous driving: A review. *IEEE Transactions on Neural Networks and Learning Systems*, 32(8):3412–3432, 2020. 1
- [44] Ye Li, Lingdong Kong, Hanjiang Hu, Xiaohao Xu, and Xiaonan Huang. Is your LiDAR placement optimized for 3D scene understanding? In *Advances in Neural Information Processing Systems*, pages 34980–35017, 2024. 1
- [45] Ao Liang, Youquan Liu, Yu Yang, Dongyue Lu, Linfeng Li, Lingdong Kong, Huaici Zhao, and Wei Tsang Ooi. LiDARCrafter: Dynamic 4D world modeling from LiDAR sequences. *arXiv preprint arXiv:2508.03692*, 2025. 2, 5, 6, 10
- [46] Venice Erin Liong, Thi Ngoc Tho Nguyen, Sergi Widjaja, Dhananjai Sharma, and Zhuang Jie Chong. AMVNet: Assertion-based multi-view fusion network for LiDAR semantic segmentation. *arXiv preprint arXiv:2012.04934*, 2020. 2
- [47] Or Litany, Alex Bronstein, Michael Bronstein, and Ameesh Makadia. Deformable shape completion with graph convolutional autoencoders. In *IEEE/CVF Conference on Computer Vision and Pattern Recognition*, pages 1886–1895, 2018. 2
- [48] Yan Liu, Qingyong Hu, Yinjie Lei, Kai Xu, Jonathan Li, and Yulan Guo. Box2Seg: Learning semantics of 3D point clouds with box-level supervision. *arXiv preprint arXiv:2201.02963*, 2022. 2
- [49] Youquan Liu, Runnan Chen, Xin Li, Lingdong Kong, Yuchen Yang, Zhaoyang Xia, Yeqi Bai, Xinge Zhu, Yuexin Ma, Yikang Li, et al. UniSeg: A unified multi-modal LiDAR segmentation network and the OpenPCSeg codebase. In *IEEE/CVF International Conference on Computer Vision*, pages 21662–21673, 2023. 2
- [50] Youquan Liu, Lingdong Kong, Weidong Yang, Xin Li, Ao Liang, Runnan Chen, Ben Fei, and Tongliang Liu. La La LiDAR: Large-scale layout generation from LiDAR data. *arXiv preprint arXiv:2508.03691*, 2025. 2, 3
- [51] Youquan Liu, Lingdong Kong, Weidong Yang, Ao Liang, Jianxiong Gao, Yang Wu, Xiang Xu, Xin Li, Linfeng



- Li, Runnan Chen, et al. Veila: Panoramic LiDAR generation from a monocular RGB image. *arXiv preprint arXiv:2508.03690*, 2025. 2, 4, 5
- [52] Zhao Liu. Super convergence cosine annealing with warm-up learning rate. In *International Conference on Artificial Intelligence, Big Data and Algorithms*, pages 1–7, 2022. 5, 10
- [53] Zhijian Liu, Alexander Amini, Sibozhu, Sertac Karaman, Song Han, and Daniela L Rus. Efficient and robust LiDAR-based end-to-end navigation. In *IEEE International Conference on Robotics and Automation*, pages 13247–13254, 2021. 1
- [54] Ilya Loshchilov and Frank Hutter. Decoupled weight decay regularization. In *International Conference on Learning Representations*, 2019. 5, 10
- [55] Alexander Lyzhov, Yuliya Molchanova, Arsenii Ashukha, Dmitry Molchanov, and Dmitry Vetrov. Greedy policy search: A simple baseline for learnable test-time augmentation. In *Conference on Uncertainty in Artificial Intelligence*, pages 1308–1317, 2020. 2
- [56] Andrey Malinin and Mark Gales. Predictive uncertainty estimation via prior networks. In *Advances in Neural Information Processing Systems*, 2018. 2
- [57] Qinghao Meng, Wenguan Wang, Tianfei Zhou, Jianbing Shen, Yunde Jia, and Luc Van Gool. Towards a weakly supervised framework for 3D point cloud object detection and annotation. *IEEE Transactions on Pattern Analysis and Machine Intelligence*, 44(8):4454–4468, 2021. 2
- [58] Andres Milioto, Ignacio Vizzo, Jens Behley, and Cyrill Stachniss. RangeNet++: Fast and accurate LiDAR semantic segmentation. In *IEEE/RSJ international conference on intelligent robots and systems*, pages 4213–4220, 2019. 7, 8, 9, 10
- [59] Kaichun Mo, Paul Guerrero, Li Yi, Hao Su, Peter Wonka, Niloy Mitra, and Leonidas J Guibas. StructureNet: Hierarchical graph networks for 3D shape generation. *arXiv preprint arXiv:1908.00575*, 2019. 2
- [60] Edgar Mauricio Munoz-Silva, Gonzalo González-Murillo, Mayra Antonio-Cruz, Juan Irving Vásquez-Gómez, and Carlos Alejandro Merlo-Zapata. A survey on point cloud generation for 3D scene reconstruction. In *International Conference on Mechatronics, Electronics and Automotive Engineering*, pages 82–87, 2021. 1
- [61] Kazuto Nakashima and Ryo Kurazume. LiDAR data synthesis with denoising diffusion probabilistic models. In *IEEE International Conference on Robotics and Automation*, pages 14724–14731, 2024. 2, 4, 5, 6, 7, 8, 9, 10
- [62] Kazuto Nakashima, Xiaowen Liu, Tomoya Miyawaki, Yumi Iwashita, and Ryo Kurazume. Fast LiDAR data generation with rectified flows. In *IEEE International Conference on Robotics and Automation*, pages 10057–10063, 2025. 2, 4
- [63] Jingcheng Ni, Yuxin Guo, Yichen Liu, Rui Chen, Lewei Lu, and Zehuan Wu. OpenDWM: Open driving world models. <https://github.com/SenseTime-FVG/OpenDWM>, 2025. 5, 6, 7, 8, 11
- [64] Kemal Oksuz, Tom Joy, and Puneet K Dokania. Towards building self-aware object detectors via reliable uncertainty quantification and calibration. In *IEEE/CVF Conference on Computer Vision and Pattern Recognition*, pages 9263–9274, 2023. 2
- [65] Adam Paszke, Sam Gross, Francisco Massa, Adam Lerer, James Bradbury, Gregory Chanan, Trevor Killeen, Zeming Lin, Natalia Gimelshein, Luca Antiga, et al. PyTorch: An imperative style, high-performance deep learning library. In *Advances in Neural Information Processing Systems*, 2019. 5, 10
- [66] Gilles Puy, Spyros Gidaris, Alexandre Boulch, Oriane Siméoni, Corentin Sautier, Patrick Pérez, Andrei Bursuc, and Renaud Marlet. Three pillars improving vision foundation model distillation for LiDAR. In *IEEE/CVF Conference on Computer Vision and Pattern Recognition*, pages 21519–21529, 2024. 2
- [67] Charles R Qi, Hao Su, Kaichun Mo, and Leonidas J Guibas. PointNet: Deep learning on point sets for 3D classification and segmentation. In *Proceedings of the IEEE conference on computer vision and pattern recognition*, pages 652–660, 2017. 2, 10
- [68] Charles Ruizhongtai Qi, Li Yi, Hao Su, and Leonidas J Guibas. PointNet++: Deep hierarchical feature learning on point sets in a metric space. In *Advances in Neural Information Processing Systems*, 2017. 2
- [69] Chao Qin, Haoyang Ye, Christian E Pranata, Jun Han, Shuyang Zhang, and Ming Liu. LINS: A lidar-inertial state estimator for robust and efficient navigation. In *IEEE International Conference on Robotics and Automation*, pages 8899–8906, 2020. 1
- [70] Rahul Rahaman et al. Uncertainty quantification and deep ensembles. In *Advances in Neural Information Processing Systems*, pages 20063–20075, 2021. 2
- [71] Haoxi Ran, Vitor Guizilini, and Yue Wang. Towards realistic scene generation with LiDAR diffusion models. In *IEEE/CVF Conference on Computer Vision and Pattern Recognition*, pages 14738–14748, 2024. 2, 5, 6, 8
- [72] Chitwan Saharia, William Chan, Saurabh Saxena, Lala Li, Jay Whang, Emily L Denton, Kamyar Ghasemipour, Raphael Gontijo Lopes, Burcu Karagol Ayan, Tim Salimans, et al. Photorealistic text-to-image diffusion models with deep language understanding. In *Advances in Neural Information Processing Systems*, pages 36479–36494, 2022. 9
- [73] Corentin Sautier, Gilles Puy, Spyros Gidaris, Alexandre Boulch, Andrei Bursuc, and Renaud Marlet. Image-to-LiDAR self-supervised distillation for autonomous driving data. In *IEEE/CVF Conference on Computer Vision and Pattern Recognition*, pages 9891–9901, 2022. 2
- [74] Murat Sensoy, Lance Kaplan, and Melih Kandemir. Evidential deep learning to quantify classification uncertainty. In *Advances in Neural Information Processing Systems*, 2018. 2
- [75] Claude E Shannon. A mathematical theory of communication. *The Bell System Technical Journal*, 27(3):379–423, 1948. 3, 9
- [76] Dong Wook Shu, Sung Woo Park, and Junseok Kwon. 3D point cloud generative adversarial network based on tree

- structured graph convolutions. In *IEEE/CVF international conference on computer vision*, pages 3859–3868, 2019. 2
- [77] Hui Shuai, Xiang Xu, and Qingshan Liu. Backward attentive fusing network with local aggregation classifier for 3D point cloud semantic segmentation. *IEEE Transactions on Image Processing*, 30:4973–4984, 2021. 2
- [78] Jiahao Sun, Chunmei Qing, Xiang Xu, Lingdong Kong, Youquan Liu, Li Li, Chenming Zhu, Jingwei Zhang, Zeqi Xiao, Runnan Chen, et al. An empirical study of training state-of-the-art LiDAR segmentation models. *arXiv preprint arXiv:2405.14870*, 2024. 1
- [79] Haotian Tang, Zhijian Liu, Shengyu Zhao, Yujun Lin, Ji Lin, Hanrui Wang, and Song Han. Searching efficient 3D architectures with sparse point-voxel convolution. In *European Conference on Computer Vision*, pages 685–702, 2020. 2, 6, 7
- [80] Antti Tarvainen and Harri Valpola. Mean teachers are better role models: Weight-averaged consistency targets improve semi-supervised deep learning results. In *Advances in Neural Information Processing Systems*, 2017. 7
- [81] Diego Valsesia, Giulia Fracastoro, and Enrico Magli. Learning localized generative models for 3D point clouds via graph convolution. In *International Conference on Learning Representations*, 2018. 2
- [82] Aaron Van Den Oord, Oriol Vinyals, et al. Neural discrete representation learning. In *Advances in Neural Information Processing Systems*, 2017. 2
- [83] Beichen Wen, Haozhe Xie, Zhaoxi Chen, Fangzhou Hong, and Ziwei Liu. 3D scene generation: A survey. *arXiv preprint arXiv:2505.05474*, 2025. 1, 2
- [84] Ryan W Wolcott and Ryan M Eustice. Visual localization within LIDAR maps for automated urban driving. In *IEEE/RSJ International Conference on Intelligent Robots and Systems*, pages 176–183, 2014. 1
- [85] Xiaopei Wu, Liang Peng, Liang Xie, Yuenan Hou, Binbin Lin, Xiaoshui Huang, Haifeng Liu, Deng Cai, and Wanli Ouyang. Semi-supervised 3D object detection with patchteacher and pillarmix. In *AAAI Conference on Artificial Intelligence*, pages 6153–6161, 2024. 2
- [86] Yang Wu, Kaihua Zhang, Jianjun Qian, Jin Xie, and Jian Yang. Text2LiDAR: Text-guided LiDAR point cloud generation via equirectangular transformer. In *European Conference on Computer Vision*, pages 291–310, 2024. 2, 5, 6
- [87] Yang Wu, Yun Zhu, Kaihua Zhang, Jianjun Qian, Jin Xie, and Jian Yang. WeatherGen: A unified diverse weather generator for LiDAR point clouds via spider mamba diffusion. In *IEEE/CVF Computer Vision and Pattern Recognition Conference*, pages 17019–17028, 2025. 2
- [88] Yuwen Xiong, Wei-Chiu Ma, Jingkan Wang, and Raquel Urtasun. UltraLiDAR: Learning compact representations for LiDAR completion and generation. *arXiv preprint arXiv:2311.01448*, 2023. 2
- [89] Chenfeng Xu, Bichen Wu, Zining Wang, Wei Zhan, Peter Vajda, Kurt Keutzer, and Masayoshi Tomizuka. SqueezeSegV3: Spatially-adaptive convolution for efficient point-cloud segmentation. In *European Conference on Computer Vision*, pages 1–19, 2020. 2
- [90] Jianyun Xu, Ruixiang Zhang, Jian Dou, Yushi Zhu, Jie Sun, and Shiliang Pu. RPNNet: A deep and efficient range-point-voxel fusion network for LiDAR point cloud segmentation. In *IEEE/CVF International Conference on Computer Vision*, pages 16024–16033, 2021. 2
- [91] Xun Xu and Gim Hee Lee. Weakly supervised semantic point cloud segmentation: Towards 10x fewer labels. In *IEEE/CVF Conference on Computer Vision and Pattern Recognition*, pages 13706–13715, 2020. 2
- [92] Xiang Xu, Lingdong Kong, Hui Shuai, Wenwei Zhang, Liang Pan, Kai Chen, Ziwei Liu, and Qingshan Liu. 4D contrastive superflows are dense 3D representation learners. In *European Conference on Computer Vision*, pages 58–80, 2024. 1
- [93] Xiang Xu, Lingdong Kong, Hui Shuai, and Qingshan Liu. FRNet: Frustum-range networks for scalable LiDAR segmentation. *IEEE Transactions on Image Processing*, 34: 2173–2186, 2025. 1, 2, 7
- [94] Xiang Xu, Lingdong Kong, Hui Shuai, Liang Pan, Ziwei Liu, and Qingshan Liu. LiMoE: Mixture of LiDAR representation learners from automotive scenes. In *IEEE/CVF Conference on Computer Vision and Pattern Recognition*, pages 27368–27379, 2025. 5, 8
- [95] Xiang Xu, Lingdong Kong, Hui Shuai, Wenwei Zhang, Liang Pan, Kai Chen, Ziwei Liu, and Qingshan Liu. Superflow++: Enhanced spatiotemporal consistency for cross-modal data pretraining. *arXiv preprint arXiv:2503.19912*, 2025. 2
- [96] Xiang Xu, Lingdong Kong, Song Wang, Chuanwei Zhou, and Qingshan Liu. Beyond one shot, beyond one perspective: Cross-view and long-horizon distillation for better LiDAR representations. In *IEEE/CVF International Conference on Computer Vision*, pages 25506–25518, 2025. 2
- [97] Yan Yan, Yuxing Mao, and Bo Li. SECOND: Sparsely embedded convolutional detection. *Sensors*, 18(10):3337, 2018. 2
- [98] Zetong Yang, Li Chen, Yanan Sun, and Hongyang Li. Visual point cloud forecasting enables scalable autonomous driving. In *IEEE/CVF Conference on Computer Vision and Pattern Recognition*, pages 14673–14684, 2024. 2
- [99] Tianwei Yin, Xingyi Zhou, and Philipp Krahenbuhl. Center-based 3D object detection and tracking. In *IEEE/CVF Conference on Computer Vision and Pattern Recognition*, pages 11784–11793, 2021. 2
- [100] Xumin Yu, Lulu Tang, Yongming Rao, Tiejun Huang, Jie Zhou, and Jiwen Lu. Point-BERT: Pre-training 3D point cloud transformers with masked point modeling. In *IEEE/CVF Conference on Computer Vision and Pattern Recognition*, pages 19313–19322, 2022. 2
- [101] Biao Zhang and Peter Wonka. Point cloud instance segmentation using probabilistic embeddings. In *IEEE/CVF Conference on Computer Vision and Pattern Recognition*, pages 8883–8892, 2021. 2
- [102] Ji Zhang, Sanjiv Singh, et al. LOAM: Lidar odometry and mapping in real-time. In *Robotics: Science and Systems*, pages 1–9, 2014. 1
- [103] Yang Zhang, Zixiang Zhou, Philip David, Xiangyu Yue, Zerong Xi, Boqing Gong, and Hassan Foroosh. PolarNet:

- An improved grid representation for online LiDAR point clouds semantic segmentation. In *IEEE/CVF Conference on Computer Vision and Pattern Recognition*, pages 9601–9610, 2020. [2](#)
- [104] Zixiang Zhou, Yang Zhang, and Hassan Foroosh. Panoptic-PolarNet: Proposal-free LiDAR point cloud panoptic segmentation. In *IEEE/CVF Conference on Computer Vision and Pattern Recognition*, pages 13194–13203, 2021. [2](#)
- [105] Dekai Zhu, Yixuan Hu, Youquan Liu, Dongyue Lu, Lingdong Kong, and Slobodan Ilic. SPIRAL: Semantic-aware progressive LiDAR scene generation. In *Advances in Neural Information Processing Systems*, 2025. [2](#)
- [106] Xinge Zhu, Hui Zhou, Tai Wang, Fangzhou Hong, Yuexin Ma, Wei Li, Hongsheng Li, and Dahua Lin. Cylindrical and asymmetrical 3D convolution networks for LiDAR segmentation. In *IEEE/CVF Conference on Computer Vision and Pattern Recognition*, pages 9939–9948, 2021. [2](#)
- [107] Zhuangwei Zhuang, Rong Li, Kui Jia, Qicheng Wang, Yuanqing Li, and Mingkui Tan. Perception-aware multi-sensor fusion for 3D LiDAR semantic segmentation. In *IEEE/CVF International Conference on Computer Vision*, pages 16280–16290, 2021. [2](#)
- [108] Vlas Zyrianov, Xiyue Zhu, and Shenlong Wang. Learning to generate realistic LiDAR point clouds. In *European Conference on Computer Vision*, pages 17–35, 2022. [2](#), [5](#), [6](#), [8](#)
- [109] Vlas Zyrianov, Henry Che, Zhijian Liu, and Shenlong Wang. LidarDM: Generative LiDAR simulation in a generated world. In *IEEE International Conference on Robotics and Automation*, pages 6055–6062, 2025. [2](#)